

Optical Identification of the *ASCA* Large Sky Survey

Masayuki Akiyama^{1,2,10,11,12}, Kouji Ohta^{2,10,11}, Toru Yamada^{3,11}, Nobunari Kashikawa⁴,
Masafumi Yagi⁴, Wataru Kawasaki^{5,12}, Masaaki Sakano^{6,12}, Takeshi Tsuru⁶, Yoshihiro
Ueda^{7,10}, Tadayuki Takahashi⁷, Ingo Lehmann^{8,10}, Günther Hasinger⁸, and Wolfgang
Voges⁹

Received _____; accepted _____

Revised Oct. 12th

¹SUBARU Telescope, National Astronomical Observatory of Japan, 650 North A'ohoku
Place, Hilo, HI, 96720, U.S.A

²Department of Astronomy, Kyoto University, Kyoto 606-8502, Japan

³Astronomical Institute, Tohoku University, Sendai 980-8578, Japan

⁴National Astronomical Observatory of Japan, Mitaka, Tokyo 181-8588, Japan

⁵Department of Astronomy, University of Tokyo, Tokyo 113-8658, Japan

⁶Department of Physics, Kyoto University, Kyoto 606-8502, Japan

⁷Institute of Space and Astronautical Science, Kanagawa 229-8510, Japan

⁸Astrophysikalisches Institut Potsdam, An der Sternwarte 16, 14482 Potsdam, Germany

⁹MPI für extraterrestrische Physik, Postfach 1603, 85740 Garching, Germany

¹⁰Visiting Astronomer, German-Spanish Astronomical Centre, Calar Alto, operated by
the Max-Planck-Institute for Astronomy, Heidelberg, jointly with the Spanish National
Commission for Astronomy

¹¹Visiting Astronomer, University of Hawaii Observatory.

¹²Research Fellow of the Japan Society for the Promotion of Science.

ABSTRACT

We present results of optical identifications of the X-ray sources detected in the *ASCA* Large Sky Survey. Optical spectroscopic observations were done for 34 X-ray sources which were detected with the SIS in the 2–7 keV band above 3.5σ . The flux limit corresponds to $\sim 1 \times 10^{-13}$ erg cm $^{-2}$ s $^{-1}$ in the 2–10 keV band. The sources are identified with 30 AGNs, 2 clusters of galaxies, and 1 galactic star. Only 1 source is still unidentified.

All of the X-ray sources that have a hard X-ray spectrum with an apparent photon index of smaller than 1 in the 0.7–10 keV band are identified with narrow-line or weak-broad-line AGNs at redshifts smaller than 0.5. This fact supports the idea that absorbed X-ray spectra of narrow-line and weak-broad-line AGNs make the Cosmic X-ray Background (CXB) spectrum harder in the hard X-ray band than that of a broad-line AGN, which is the main contributor in the soft X-ray band. Assuming their intrinsic spectra are same as a broad-line AGN (a power-law model with a photon index of 1.7), their X-ray spectra are fitted with hydrogen column densities of $\log N_{\text{H}}(\text{cm}^{-2}) = 22 \sim 23$ at the object's redshift. On the other hand, X-ray spectra of the other AGNs are consistent with that of a nearby type 1 Seyfert. In the sample, four high-redshift luminous broad-line AGNs show a hard X-ray spectrum with an apparent photon index of 1.3 ± 0.3 . The hardness may be explained by the reflection component of a type 1 Seyfert. The hard X-ray spectra may also be explained by absorption with $\log N_{\text{H}}(\text{cm}^{-2}) = 22 \sim 23$ at the object's redshift, if we assume an intrinsic photon index of 1.7. The origin of the hardness is not clear yet.

Based on the logN-logS relations of each population, contributions to the CXB in the 2–10 keV band are estimated to be 9% for less-absorbed AGNs ($\log N_{\text{H}}(\text{cm}^{-2}) < 22$) including the four high-redshift broad-line AGNs with a

hard X-ray spectrum, 4% for absorbed AGNs ($22 < \log N_{\text{H}}(\text{cm}^{-2}) < 23$, without the four hard broad-line AGNs), and 1% for clusters of galaxies in the flux range from $3 \times 10^{-11} \text{ erg cm}^{-2} \text{ s}^{-1}$ to $2 \times 10^{-13} \text{ erg cm}^{-2} \text{ s}^{-1}$. If the four hard broad-line AGNs are included in the absorbed AGNs, the contribution of the absorbed AGNs to the CXB is estimated to be 6%.

In optical spectra, there is no high-redshift luminous cousin of a narrow-line AGN in our sample. The redshift distribution of the absorbed AGNs are limited below $z = 0.5$ excluding the four hard broad-line AGNs, in contrast to the existence of 15 less-absorbed AGNs above $z = 0.5$. The redshift distribution of the absorbed AGNs suggests a deficiency of AGNs with column densities of $\log N_{\text{H}}(\text{cm}^{-2}) = 22$ to 23 in the redshift range between 0.5 and 2, or in the X-ray luminosity range larger than $10^{44} \text{ erg s}^{-1}$, or both. If the large column densities of the four hard broad-line AGNs are real, they could complement the deficiency of X-ray absorbed luminous high-redshift AGNs.

Subject headings: surveys — galaxies: active — quasars: general —
X-rays:galaxies — diffuse radiation

1. Introduction

Since the discovery of the cosmic X-ray background (CXB) by Giacconi et al. (1962) in the 2–6 keV band, many efforts have been made to understand the origin of the CXB. Recently in *ROSAT* deep surveys, 70 – 80% of the CXB in the 0.5–2 keV band has been resolved into discrete sources at a flux limit of 1×10^{-15} erg cm⁻² s⁻¹ (Hasinger et al. 1998). Within the flux level of the deep survey, broad-line AGNs are the dominant population and the main contributor to the CXB in the 0.5–2 keV band. On the other hand, in the harder 2–10 keV band, only $\sim 3\%$ of the CXB was resolved into discrete sources (Piccinotti et al. 1982) before *ASCA* surveys. Broad-line AGNs have X-ray power-law spectra with a photon index of $\Gamma = 1.7$ in the 2–10 keV band (Turner & Pounds 1989) which are significantly softer than that of the CXB in that band ($\Gamma = 1.4 \sim 1.5$; Gendreau et al. 1995; Ishisaki et al. 1999), thus there must be objects which have harder X-ray spectra than nearby broad-line AGNs and contribute significantly to the CXB in the hard band.

Resolving the hard X-ray sky is a direct way to reveal the nature of X-ray sources in the hard band. *ASCA* GIS observations of three *ROSAT* Deep PSPC Fields down to the 5×10^{-14} erg cm⁻² s⁻¹ have been done so far (Georgantopoulos et al. 1997; Boyle et al. 1998a). However, because of the large positional uncertainties of the GIS-selected X-ray sources, a large fraction of hard X-ray selected sources is still unidentified; the nature of hard X-ray sources and the difference from the *ROSAT* selected objects are still unclear.

Based on the unified scheme of AGNs, absorbed AGNs are proposed as candidates for the hard X-ray sources (Comastri et al. 1995; Madau, Ghisellini, & Fabian 1994). Because of absorption of soft X-ray photons by obscuring material, they have harder X-ray spectra than type 1 AGNs. To reproduce the CXB spectrum, it is argued that there are around three times more absorbed AGNs than non-absorbed AGNs in the universe and absorbed AGNs dominate the CXB above 2 keV. In consequence of the assumption, the existence

of absorbed narrow-line QSO (so called type 2 QSO) is expected. From optical follow-up observations of X-ray surveys in the soft and hard bands, several luminous narrow-line AGNs have been found at intermediate to high redshift universe (e.g., Stocke et al. 1982; Almaini et al. 1995; Ohta et al. 1996; Boyle et al. 1998b; Barcons et al. 1998; Schmidt et al. 1998). On the other hand, existence of red *broad-line* QSOs whose red color suggests absorption to its nucleus was reported from a radio survey (Webster et al. 1995). Such a population was also identified in *ROSAT* surveys (Kim & Elvis 1999) and *Beppo-SAX* surveys (Fiore et al. 1999), but X-ray spectra, number densities and contributions to the CXB of both of these narrow-line and red broad-line QSOs are not clear.

To reveal the nature of X-ray sources in the hard band, studies on a well-defined sample are important. We are now conducting an unbiased large and deep survey with *ASCA* in the region near the north Galactic pole, i.e., *ASCA* Large Sky Survey (hereafter LSS; Inoue et al. 1996; Ueda 1996; Ueda et al. 1998; Ueda et al. 1999a (Paper I)). The flux limit of the LSS ($\sim 1 \times 10^{-13}$ erg cm $^{-2}$ s $^{-1}$ in the 2–10 keV band) is 100 times deeper than the *HEAO1* A2 survey, which was the deepest systematic survey in the hard band (Piccinotti et al. 1982) before *ASCA*. We have surveyed 7.0 deg 2 and 5.4 deg 2 with the GIS and the SIS detectors, respectively. Combining the data from the GIS and the SIS, we detected 44 sources in the 2–10 keV band with the following criteria: 1) the significance of summed count rate of the GIS and the SIS should exceed 4.5, and 2) the significance of either the GIS or the SIS should also exceed 3.5 (Paper I). They correspond to 20 – 30% of the CXB in this band. The advantages of the sample are 1) the survey area as a function of limiting count rates was determined well by simulations, 2) accurate X-ray positions were determined by using the SIS whose resolution is higher than the GIS and by correcting the temperature-dependent misalignment between the focal plane detectors and the attitude sensors, and 3) the X-ray spectrum of each source was determined by fitting power-law model with the Galactic absorption to the GIS and the SIS data simultaneously

in the 0.7–10 keV band (Paper I). Determining their X-ray spectra is important not only to know their X-ray properties but also to know the flux limit of the survey, because the limit varies with the X-ray spectrum of each source. The average of the apparent photon index of the 36 X-ray sources detected in the flux range between 0.8×10^{-13} and 4×10^{-13} erg cm⁻² s⁻¹ is $\Gamma = 1.49 \pm 0.1$ (Paper I), which is significantly harder than the spectra of X-ray sources detected in shallower surveys in the 2–10 keV band and close to that of the CXB. Identification of these sources is clearly important to understand the nature of hard X-ray sources and the origin of the CXB.

In this paper, we report results of optical identifications of X-ray sources detected in the hard band with the SIS in the *ASCA* LSS. The sample definition and selections of optical candidates are discussed in Section 2, results of optical spectroscopy for the selected candidates and reliability of the identifications are presented in Section 3, and optical and X-ray spectroscopic properties of identified objects are described in Section 4. The contribution of the population to the CXB and the redshift distribution of the AGNs are discussed in Section 5 and 6, respectively. In Section 7, we present multi-wavelength properties of the identified AGNs. Throughout this paper, we use $q_0 = 0.5$ and $H_0 = 50$ km s⁻¹ Mpc⁻¹. We call each X-ray source with the exact name and the identification number, like AX J132032+3326(227), for convenience.

2. Observations

2.1. The X-ray Survey Observations and the Sample Definition

To minimize the effect of the galactic absorption and contamination from bright X-ray sources, the survey area was defined as a continuous region of ~ 5 degree² near the north Galactic pole, centered at $\alpha=13^{\text{h}}14^{\text{m}}$, $\delta=31^{\circ}30'$ (J2000). Seventy-six pointings of the

survey-observations were done from Dec. 1993 to Jul. 1995. These exposures were designed to evenly cover the whole survey region with a 20 ksec effective exposure of the SIS. The source detections were done with the SIS data in the 0.7–7 keV, 0.7–2 keV, and 2–7 keV bands and the GIS data in the 0.7–7 keV, 0.7–2 keV, and 2–10 keV bands. For details of the survey observation, source extraction, and spectral fitting, including the survey region and the position of the sources on the sky, see Paper I.

In this paper, we concentrate on the 34 X-ray sources detected with the SIS in the 2–7 keV band above 3.5σ (hereafter, the SIS 2–7 keV 3.5σ sample). Table 1 shows the survey area as a function of limiting count rates for the sample. The typical and the deepest limiting count rates of the sample are 2 counts ksec^{-1} and 1.2 counts ksec^{-1} , respectively. They correspond to 1.8×10^{-13} $\text{erg cm}^{-2} \text{s}^{-1}$ and 1.1×10^{-13} $\text{erg cm}^{-2} \text{s}^{-1}$ in the 2–10 keV band for an X-ray source with a power-law spectrum with a photon index of 1.7. All X-ray sources in the SIS 2–7 keV 3.5σ sample have the significance level larger than 4.5 in summed count rate of the GIS and the SIS in both of the 0.7–7 keV and 2–7 keV bands and the positional uncertainties of such sources were estimated to be 0'6 in radius with the 90% confidence level (Paper I). The number of spurious sources was estimated to be at most a few percent (Paper I), thus less than 1 spurious source was expected to be in the SIS 2–7 keV 3.5σ sample.

EDITOR: PLACE TABLE 1 HERE.

2.2. Optical Imaging Observations and Selections of Optical Counterpart Candidates

AGNs are the most plausible optical counterparts for the majority of the X-ray sources, thus at least we have to reach the optical flux limit which is converted from the deepest X-ray

flux limit based on X-ray-to-optical flux ratio of AGN. If we assume power-law spectra with an X-ray photon index of 1.7 and an optical energy index of -0.5 together with the X-ray-to-optical flux ratio of AGNs identified in the *ROSAT* Deep Survey (Schmidt et al. 1998), the expected optical magnitude for the optical counterpart of an X-ray source with 1.1×10^{-13} erg cm $^{-2}$ s $^{-1}$ in the 2–10 keV band is $R = 16 \sim 21$ mag.

Candidates of optical counterparts were mainly selected from the APM catalog which is obtained from scans of glass copies of the Palomar Observatory Sky Survey plate (McMahon et al. 1992). However, the limiting magnitude of the catalog is $R \cong 20$ mag and is not deep enough to pick up optical counterparts for faint X-ray sources. To complement the depth of the data, we made imaging observations of the LSS region at the KISO 1.05m Schmidt telescope in March and April 1994. In these observations, we used the mosaic CCD camera (Sekiguchi et al. 1992) which is made up of 15 1024 \times 1024 CCD chips and covers 2 \times 5 degree 2 with 15 shots. The spatial resolution in the setup was 0 $''$.75 pix $^{-1}$. Images were taken in the R band with an exposure time of 20 minutes. The reduction of the data was done by the usual method for optical imaging data. The weather condition during the observation was neither stable nor photometric and the limiting magnitude changed from field to field. The typical seeing was 4 $''$ (FWHM) and the typical limiting magnitude was $R \cong 21$ mag, about one magnitude deeper than the APM data.

There are several optical objects within each error circle of X-ray source above $R = 21$ mag. Two X-ray sources (AX J132032+3326(227) and AX J130748+2925(002)) show clear excesses of galaxies in and around their error circles (see Figure 1). These two objects have been cataloged as candidate clusters of galaxies, Abell 1714 (Abell, Corwin, & Olowin 1989) and Zwcl 1305.4+2941 (Zwicky, Herzog, & Wild 1961), respectively. Zwcl 1305.4+2941 was also detected in the *Einstein* Medium Sensitivity Survey and its redshift was determined to be $z=0.241$ (Stocke et al. 1991). We took deeper and better resolution images with a

Tektronix 2048× 2048 CCD on the University of Hawaii 88" telescope on 1995 March and 1996 April in the *R* and *I* band and confirmed the excess of galaxies. Thus, we identified the two sources with clusters of galaxies. For other sources, active galaxies are the most plausible counterparts. From optical objects within 0'.8, which is slightly larger than the estimated 90% confidence error radius (0'.6), of each X-ray source, we selected targets for spectroscopy, using 1) deeper X-ray follow-up data in the soft and hard band, 2) radio emission, and 3) blueness of UV or optical color which indicate existence of an activity in a object.

2.2.1. Deep Follow-up Observations in X-ray band

To pinpoint optical counterparts of X-ray sources, 20 ksec follow-up observations were made with the *ROSAT* HRI in 2 fields in December 1997. We selected two fields centered at $\alpha=13^{\text{h}}14^{\text{m}}36^{\text{s}}$, $\delta=32^{\circ}01'12''$ and $\alpha=13^{\text{h}}12^{\text{m}}29^{\text{s}}$, $\delta=31^{\circ}13'12''$ (J2000) with a radius of 19', to cover as many *ASCA* sources as possible. We summarize the data reduction and the source detection in Appendix A. All of the X-ray sources in the SIS 2–7 keV 3.5σ sample (AX J131521+3159(136), AX J131407+3158(127), and AX J131327+3155(121) in the former field, and AX J131249+3112(096), AX J131128+3105(080), and AX J131321+3119(103) in the latter field) except one (AX J131345+3118(104)) in these fields were detected by the HRI and their optical counterparts were pinpointed thanks to the 5" positional accuracy of the HRI. On the position of the missed source (AX J131345+3118(104)), there is an X-ray peak in the HRI image, though the significance level is slightly lower than the detection limit. Since there is also an optical object at the position, the X-ray source is pinpointed. It should be noted that there is no hard X-ray source which has an X-ray spectrum with an apparent photon index smaller than 1.0 in these HRI observed fields.

Deep 40 ~ 100 ksec pointing observations for 4 sources, which have hard X-ray

spectra, (AX J131501+3141(119), AX J131551+3237(171), AX J131210+3048(072), and AX J130926+2952(016)) were made by *ASCA* and more precise positions and X-ray spectra were obtained (Sakano et al. 1998; Sakano et al. 1999; Ueda et al. 1999b). The error circles for these sources were estimated to be less than $0.6'$ at a 90% confidence level.

By the *ROSAT* PSPC, 15 and 13 *ASCA* LSS sources were detected in the *ROSAT* PSPC All-Sky Survey (Voges et al. 1999) and pointing observations (Voges, private communication), respectively. 9 of them were detected in both of the observations, thus the X-ray positions of 19 *ASCA* sources were determined accurately. In details of the cross-identification, see Appendix B.

2.2.2. Cross-correlation with *FIRST* radio source catalog

In the course of the optical counterpart selection, we examined the distribution of *FIRST* radio sources around LSS X-ray sources to evaluate the cross-correlation between radio and X-ray sources. The *FIRST* survey is a radio source survey conducted with the Very Large Array in the 1.4 GHz band with a 5σ limiting flux of 1 mJy (Becker, White, & Helfand 1995). There are 17 radio sources within $0.5'$ from the centers of the X-ray sources; by contrast no radio source exists between $0.5'$ and $1'$ from them. Based on the surface number density of detected radio sources in the LSS field, the contamination of a radio source which is not an counterpart of an X-ray source is expected to be less than 1 source for the whole 34 X-ray sources within $0.5'$. Thus, the 17 radio sources are likely radio-counterparts of X-ray sources. In details of the cross-identification, see Appendix B. Three X-ray sources have two to four radio sources within $0.5'$. They are thought to be radio-loud objects with radio lobes or clusters of galaxies. One of the three X-ray sources is already identified with a cluster of galaxies (AX J132032+3326(227)). In summary, 35% (12/34) of the SIS 3.5σ sample are detected in the *FIRST* survey and an optical counterpart is pinpointed thanks to

the good positional accuracy ($1''$) of the FIRST catalog, except for AX J131639+3149(137). For the X-ray source, there is no optical object within an error circle of the FIRST radio source (see notes in Section 3.1). In the error circle of AX J131529+3117(110), there is a radio peak with a flux of 0.63 mJy which is slightly lower than the detection limit of the FIRST. Because there is an optical object at the position, we identified the optical object with the counterpart of the radio peak and the X-ray source.

The high fraction of radio-detected X-ray sources in comparison with other results (e.g., 10% in De Ruiter et al. 1997) is due to a match between the flux limit of the VLA FIRST 1.4 GHz survey and that of the LSS; the ratio of the flux limits is one order of magnitude larger than the typical radio-to-X-ray flux ratio of *radio-quiet* broad-line AGN (Elvis et al. 1994) but within the scatter of the ratio of the *radio-quiet* population. Thus, not only radio-loud AGNs but also some radio-quiet AGNs are included in the LSS-FIRST sample (see Section 7.2). It is worth noting that radio emission is transparent against obscuring material, thus obscured AGNs are detected in the radio wavelength as well as in the hard X-ray band, in an unbiased way.

2.2.3. UV and Optical Color

Based on the results of the optical identification in soft X-ray surveys, a broad-line AGN is a plausible optical counterpart for a part of X-ray sources detected in the hard band and they can be selected by a blueness of their UV or optical color if they are at redshift smaller than 3. There are two UV-excess surveys which cover the southern half ($\delta < 32^{\circ}10'$) of the LSS. These are Usher (1981) and Moreau & Reboul (1995). Objects with an $U - V$ color bluer than 0.0 down to $B = 20$ mag and 0.1 down to $V = 20$ mag are cataloged in the former and the latter, respectively. 8 out of 20 X-ray sources in the area have one or two UV-excess object(s) within $0'.8$ in total. 6 are also detected in the X-ray follow-ups with

ROSAT HRI or in the FIRST survey. Considering the number density of UV-excess objects in Moreau & Reboul (1995), the expected number of contamination within 0'8 from the center of the 20 X-ray sources is calculated to be 0.5, thus all 8 correlated objects can be considered as plausible optical counterparts of X-ray sources. Such a low probability of contamination indicates that there is no serious bias to selecting an UV excess object which is not a true optical counterpart of an X-ray source. Additionally, two galaxies in the 0'8 radii of AX J131805+3349(233) are cataloged as UV-excess galaxies in the KUG catalog (Takase & Miyauchi-Isobe 1986).

To select candidates of broad-line AGNs with fainter magnitude and to cover the whole LSS area, we also picked up objects with $B - R < 1.0$ mag as a broad-line AGN candidates in the whole area, assuming a typical color of broad-line QSOs ($B - R = 0.52$ mag; Richstone & Schmidt 1980) with a dispersion of distribution ($\Delta B - R = 0.2$ mag) and an error of photometry ($\Delta B - R = 0.3$ mag). The APM $O - E$ color was converted to the $B - R$ color with $(O - E)_{\text{APM}} = 1.135 \times (B - R)$ (Evans 1989). 19 X-ray sources have one or two optical object(s) which meet the above criteria within 0'8. 5 of them are also detected in either the X-ray follow-ups with *ROSAT* HRI or in the FIRST survey. Within 0'6 and between 0'6 and 0'8 from the 34 X-ray sources, there are 19 and 6 blue objects, respectively. Based on the number density of objects with $B - R$ color bluer than 1.0 in the APM catalog, the expected number of contamination of blue objects which are not X-ray source is estimated to be 6 and 5 in the inner circles and outer annuli, respectively. Thus, two thirds of the blue objects in the inner circles are expected to be true optical counterpart of X-ray sources, on the other hand, most of the blue objects in the outer annuli are thought to be contamination of non-X-ray objects.

Almost all (5 out of 6) the hard X-ray sources which have a photon index smaller than 1.0 have no such blue object within their error circles; therefore an optical counterpart

different from a broad-line AGN is suggested. This tendency is the same as the previous results reported in Akiyama et al. (1998b), but the new result is more significant than the previous one, because we concentrate on brighter X-ray sources whose positions and X-ray photon indices were determined well and more accurate X-ray positions were obtained for each X-ray source by correcting for the temperature effect in the satellite acquisition as mentioned in Section 2.1.

In summary, except for 2 clusters of galaxies, 24 sources were pinpointed by X-ray follow-ups with the *ROSAT* HRI or PSPC or radio detections, 5 more sources have only one object which is selected by its blue optical color, and the remaining 3 sources have no optical counterpart which meets the above criteria. For these 3 sources, we picked up the brightest optical object within each error circle as a primary target. The list of the selected objects is shown in Table 2 and, in finding charts of Figure 1, they are labeled with “A”, “B”, and “C” in order of distance from the X-ray centroid. Additionally, we listed some objects which were not selected by the above methods but observed in the optical spectroscopy. These objects were indicated with a label “Z”.

EDITOR: PLACE TABLE 2 HERE.

2.3. Optical Spectroscopy

We made spectroscopic observations for the optical-counterpart candidates which are selected based on the above criteria with the highest priority. Spectroscopic observations were made with the University of Hawaii 88” telescope on March 1998, except for the hardest source (AX J131501+3141(119)), a candidate of galactic star (AX J131850+3326(219)), and the two clusters of galaxies. We used the Wide Field Grism Spectrograph with a grating of 420 rulings mm^{-1} and the blaze wavelength of 6400Å. The spatial resolution was

$0.''354 \text{ pixel}^{-1}$ and the seeing during the observation was $0.''8 \sim 1''$. A slit width of $1.''2$ was used. The spectral coverage ranges from 4000\AA to 9000\AA and the spectral resolution, which is measured by the HgAr lines in comparison frames and night-sky lines in object frames, is 12\AA (FWHM). We also took imaging data of each X-ray source with a better angular resolution without filter for finding charts.

We have also done spectroscopic observations with the 3.5m telescope at Calar Alto observatory for a candidate galactic star (AX J131850+3326(219)) and three objects (AX J131831+3341(228), AX J130840+2955(014), and AX J131639+3149(137)) which were already observed in the previous run. We used the MOSCA instrument in a single-slit mode with a g250 grating which has $250 \text{ rulings mm}^{-1}$ and a blaze wavelength of 5700\AA . The spectral coverage ranges from 4000\AA to 8000\AA . In the configuration, the sampling was $5.95 \text{\AA pixel}^{-1}$. A slit width of $1.''5$, which was the same as the FWHM of the seeing, was used. Thus, the spectral resolution was 22\AA (FWHM), which was estimated by measuring widths of night sky lines in object frames. The spatial resolution was $0.''32 \text{ pixel}^{-1}$.

For the hardest X-ray source (AX J131501+3141(119)), we made spectroscopic observations with the Kitt Peak National Observatories Mayall 4m and 2.1m telescopes. For details of the observations, see Akiyama et al. (1998a).

The data were analyzed using IRAF.¹³ After bias subtraction, flat-fielding, and wavelength calibration, optimum extraction method by **apextract** package was used to extract one dimensional spectral data from the two dimensional original data. For the UH data, flux calibrations were done with Feige 34. The flux calibrations did not work well in

¹³ IRAF is distributed by the National Optical Astronomy Observatories, which is operated by the Association of Universities for Research in Astronomy, Inc. (AURA) under cooperative agreement with the National Science Foundation.

the wavelength larger than 7000\AA and for some data in the wavelength shorter than 5000\AA taken at very large zenith distances. For the Calar Alto data, flux calibrations were done with HD84937. The data were affected by fringes in the wavelength longer than 7000\AA . Spectral fitting for emission lines was made by the χ^2 minimization method with **specfit** command in **spfitpkg** package in the IRAF. FWHMs of line widths were deconvolved by the spectral resolution shown above.

3. Results and Reliability

3.1. Results of Optical Identification

Many (25 out of 34) X-ray sources have one optical-counterpart candidate which shows broad permitted-emission lines whose FWHM is larger than those of forbidden-emission lines or 1000 km s^{-1} in their optical spectra. The detected broad lines and line widths are summarized in Table 3. This suggests that most of the X-ray sources originate from AGNs.

In the remaining sources, 5 X-ray sources have only an object with narrow-emission lines. For 4 of them (AX J131758+3257(195), AX J131551+3237(171), AX J131501+3141(119), AX J131210+3048(072)), both the $H\alpha$ and $H\beta$ regions were observed. We classified these objects, using the [NII] 6583\AA -to- $H\alpha$ and [OIII] 5007\AA -to- $H\beta$ line ratios (Osterbrock 1989). All of them show strong [NII] 6583\AA line as well as an $H\alpha$ line and they fall in the region occupied by AGNs. For the remaining one object, AX J130840+2955(014), spectroscopic observations cover only the $H\beta$ emission line region, because of atmospheric absorption and fringes. It has a large [OIII] 5007\AA -to- $H\beta$ flux ratio and the existence of an AGN is suggested, but the ratio is not large enough to exclude possibility of star-forming galaxy. However, the spectrum shows optical continuum which is dominated by old stellar populations and there is no indication of star-formation activity. Thus, the object is also

identified with AGN.

We list notes on problematic cases, below.

AX J131054+3004(037) The FIRST source (A in Figure 1) in the error circle was identified with a narrow-line AGN at a redshift of 0.245. There is also a blue object within the error circle (B) and it was identified with a broad-line AGN at a redshift of 1.577. Because most other X-ray sources whose X-ray spectra are similar to this X-ray source were identified with broad-line AGNs, we assigned the broad-line AGN as the optical counterpart of the X-ray source. It is possible that the narrow-line AGN or both is the origin of the X-ray source.

AX J131639+3149(137) At the position of the FIRST source in the error circle ($\alpha=13^{\text{h}}16^{\text{m}}38.9^{\text{s}}$, $\delta=31^{\circ}49'57.8''$), no optical object brighter than $R = 22.5$ mag can be seen. The nearest object, which is separated by $14''$ from the radio position and has a blue color, was identified with a broad-line AGN at $z=0.622$. The projected distance between radio and optical source corresponds to 108 kpc at the redshift. If we assume that the radio emission is originated from the object, the radio-to-X-ray flux ratio corresponds to that of radio-loud objects (see Section 7.2).

AX J131832+3259(199) The brightest stellar object (A in Figure 1) in the $0'.8$ error circle was identified with a G-type star. Based on an X-ray-to-optical flux ratio of a G-type star, this object cannot be the origin of the X-ray source. This source is not identified yet.

As a result, 34 X-ray sources in the SIS 2–7 keV 3.5σ sample were identified with 30 AGNs including 5 objects with only narrow-emission lines, 2 clusters of galaxies, and 1 galactic star. Only 1 source is still unidentified. There are 2 X-ray sources which have HII-region like galaxies in their error circles. But they also have an optical counterpart

candidate with AGN activity, thus we identified the X-ray sources with the AGNs. The resulting identification and classification for each X-ray source is indicated with bold characters in Table 2. The optical spectra of the identified objects are shown in Figure 1. Detected broad-lines in each object are listed in Table 3. Physical parameters of the identified objects are summarized in Table 4. In the next 2 subsections, we discuss the reliability of the identifications.

EDITOR: PLACE FIGURE 1 HERE.

EDITOR: PLACE TABLE 3 HERE.

EDITOR: PLACE TABLE 4 HERE.

3.2. Contamination

Figure 2 shows the distribution of optically identified objects in the X-ray error circles. Almost all X-ray sources were identified with optical objects within $0'.6$, though we picked up the candidates within $0'.8$. This result confirms the estimated 90% confidence error radius of $0'.6$.

We have checked the reliability of our identification by estimating chance contaminations in the error circle. Based on number counts of optically-selected broad-line AGN brighter than $B = 21.0$ mag with a redshift smaller than 3 (Hartwick and Schade 1990), the expected number of chance contaminations of broad-line AGN within 34 error circles is 0.29 and is negligible. For narrow-line AGNs, 3/5 of them, are pinpointed by the FIRST radio survey

and chance contamination is very small for the sample as mentioned above. Therefore contamination of an object which is not an X-ray source is very low.

EDITOR: PLACE FIGURE 2 HERE.

3.3. X-ray-to-optical Flux Ratio of the Identified Objects

An X-ray-to-optical flux ratio is one of useful tools to check the reliability of identification. To compare the X-ray-to-optical flux ratios of identified objects with $\log f_X/f_V$ of the *Einstein* Medium Sensitivity Survey (EMSS) sample (Stocke et al. 1991), we plot the relation between optical magnitude and hard X-ray flux in Figure 3. To plot the equal $\log f_X/f_V$ lines, we converted the *V* band magnitude to the *R* band magnitude and 0.3–3.5 keV flux to 2–10 keV flux for the EMSS sample, using a $V - R$ color of 0.22 mag, which is equivalent to a typical optical energy index of broad line AGNs (-0.5) and a photon index of 1.7 in the 0.3–10 keV band, respectively. The $\log f_X/f_V$ values of the EMSS AGNs, clusters of galaxies, and galactic G-type stars are distributed -1.0 to $+1.2$, -0.5 to $+1.5$, and -4.3 to -2.4 (Stocke et al. 1991), respectively. In the fainter flux range, the AGNs detected in the *ROSAT* HRI Lockman Hole survey also occupy the same value of $\log f_X/f_V$ (Schmidt et al. 1998). The $\log f_X/f_V$ values of the identified AGNs, clusters of galaxies, and a galactic star in our sample are consistent with the distribution of the EMSS sample. The consistency of $\log f_X/f_V$ with the EMSS objects supports the reliability of the identification in the LSS sample.

However, there are two AGNs which have values of $\log f_X/f_V$ slightly outside of the EMSS sample. One AGN (AX J131831+3341(228)) has a $\log f_X/f_V$ value of $+1.3$, which is X-ray louder than the EMSS AGNs. The AGN has a strong narrow [OIII] 5007Å line compared with the broad H β line. Thus, the large $\log f_X/f_V$ value might be explained

by an optical absorption of its nucleus. The other AGN (AX J131805+3349(233)), whose $\log f_X/f_V$ is smaller than -1.0 , is dominated by its host galaxy in the optical light (see Figure 1) and this component makes the object optically brighter in comparison with other AGNs. The lower limit of $\log f_X/f_V$ on the optical counterpart of the unidentified source, AX J131832+3259(199), is $\sim +1$. This value is consistent with that of the EMSS AGNs.

EDITOR: PLACE FIGURE 3 HERE.

4. Optical and X-ray Spectral Properties of the Identified AGNs

4.1. Strength of Broad Emission Lines

To examine the strengths of broad-lines in comparison with narrow-lines, we measured the equivalent width ratios of *broad plus narrow permitted lines-to-a narrow forbidden line*. For objects at low redshifts, we measured the equivalent width ratios of $H\alpha$ -to-[NII] 6583Å and $H\beta$ -to-[OIII] 5007Å. For objects at redshifts between 0.3 and 0.75, we could measure only $H\beta$ -to-[OIII] 5007Å ratio (we could not measure the ratio of AX J131639+3149(137), because of the fringe effect, thus the object is included in the higher redshift sample). The results are summarized in Table 3 and shown in Figure 4. The objects with strong broad $H\alpha$ and $H\beta$ lines occupy the upper-right region of the figure. Most objects at redshifts lower than 0.3 do not show significant broad component in the $H\beta$ line and are placed in the lower part. About half of them show a broad component in the $H\alpha$ line and are distributed in the lower-right region. In the right box, among objects with redshifts between 0.3 and 0.75, most of the objects show significant broad component in the $H\beta$ line. In this redshift range, the fraction of objects with large $H\beta$ -to-[OIII] 5007Å ratio is larger than the lower redshift sample in the left box. Based on the criteria used in Winkler (1992), the upper

and lower boundary of the $H\beta$ -to-[OIII] 5007Å ratio distribution in our sample correspond to type 1.2 and type 1.8 \sim 2 Seyfert, respectively.

All 11 objects at redshift above 0.75 and AX J131639+3149(137) show broad MgII 2800Å or MgII 2800Å and CIII] 1909Å lines. The equivalent widths and the line widths of their MgII 2800Å lines are summarized in Table 3. Their equivalent widths are consistent with those of a composite spectrum of optically-selected QSOs ($50 \pm 29\text{\AA}$; Francis et al. 1991). AX J131707+3237(175) and AX J131021+3019(039) have a narrow-emission component in the MgII 2800Å and CIII] 1909Å, respectively. Their line widths are as large as 1400 km s^{-1} in FWHM and significantly larger than line widths of typical narrow-lines. Thus, there is no high-redshift luminous cousin of a narrow-line AGN in our sample. Such a deficiency of luminous narrow-line AGN is also reported in a radio selected sample of AGN (e.g., Lawrence 1991) and a far-infrared selected sample (e.g., Barcons et al. 1995).

EDITOR: PLACE FIGURE 4 HERE.

4.2. X-ray Spectral Properties and the Effect of Absorption

The distribution of the apparent photon indices of the identified objects determined in the 0.7–10 keV band as a function of redshift is shown in Figure 5. All X-ray sources which have an apparent photon index smaller than 1 are identified with AGNs at redshifts smaller than 0.5. In the previous Figure 4, we mark the X-ray sources which have photon indices smaller than 1 with dots. AX J131551+3237(171), AX J131501+3141(119), AX J131210+3048(072), and AX J130840+2955(014) were identified with AGNs which show no significant broad line in $H\alpha$ and $H\beta$. Among them, the hardest source, AX J131501+3141(119), is identified with a type 2 Seyfert at $z=0.072$ (Akiyama et al. 1998a; Sakano et al. 1998). The remaining hard X-ray source (AX J130926+2952(016)) was identified with an AGN which shows a weak

broad $H\beta$ line and has a small $H\beta$ -to- $[OIII]5007\text{\AA}$ ratio. Thus, the object corresponds to a type 1.8 Seyfert (Winkler 1992). These identifications support the picture (e.g., Comastri et al. 1995) that the absorbed X-ray spectrum of narrow-line and weak-broad-line AGNs make the CXB spectrum harder than X-ray spectrum of broad-line AGN in the hard band. There still remains one hard source with a photon index of 0.58 unidentified.

EDITOR: PLACE FIGURE 5 HERE.

Photon indices of other AGNs are distributed in the range from 1.2 to 2.1. There are three broad-line AGNs with an apparent photon index as small as 1.4 at intermediate to high redshifts. A dashed line in the figure shows the expected change of the *apparent* photon index in the 0.7–10 keV band with redshift for a type 1 Seyfert. It is derived by fitting a power-law model to the redshifted average X-ray spectrum of type 1 Seyferts (Gondek et al. 1996) in the 0.7–10 keV band. Because of the reflection component, the observed photon index of type 1 Seyfert in the 0.7–10 keV band is expected to get harder to $z \sim 2$ and to reach a minimum photon index of 1.4 at a redshift of 2.5. The photon index distribution of the broad-line AGN sample is consistent with this line. Thus, the hardness of the apparent photon indices of the three high-redshift broad-line AGNs may be explained by the existence of the reflection component. It should, however, be noted that the existence and the strength of a reflection component in AGNs with a luminosity of 10^{45} erg s^{-1} is not confirmed, so far.

For the AGNs, we also fitted their X-ray spectra with an absorbed power-law model, assuming absorbing matter at the object’s redshift and an intrinsic photon index of 1.7. The results are shown in column 8 of Table 4 and shown in Figure 6 as a function of X-ray luminosities. The upper boundary of the distribution of the column density is consistent with an estimated limit on the column density in the LSS sample (see, Section 6). Hard

X-ray sources which were identified with narrow-line or weak-broad-line AGNs at redshift smaller than 0.5 are fitted with column densities of $\log N_{\text{H}}(\text{cm}^{-2}) = 22 \sim 23$. Most of the other AGNs are fitted with column densities less than $\log N_{\text{H}}(\text{cm}^{-2}) = 22$. However, four high-redshift ($2 > z > 0.5$) luminous ($L_{2-10 \text{ keV}} = 10^{44.5 \sim 45.5} \text{ erg s}^{-1}$) broad-line AGNs (AX J131816+3240(183), AX J131054+3004(037), AX J131724+3203(152), and AX J131021+3019(039)) are fitted with large column densities. Such large neutral hydrogen column densities conflict with the existences of broad MgII lines and strong UV continua in their optical spectra. However, there is a possibility that optical extinction is not always strongly correlated with X-ray absorption (e.g., NGC4151), as in the case where the X-ray absorbing gas is located within the dust sublimation radius, the absorbing column density is variable, or if the gas-to-dust ratio or the composition is different from the Galactic interstellar gas. These hardness may also be explained by the effect of the reflection component. The presence of the reflection component makes observed type 1 AGN spectrum harder than a photon index of 1.7 in the 0.7–10 keV band at high-redshift, as shown in Figure 5. The slightly hardened X-ray spectrum in the observed band is spuriously fitted with large column density in the rest-frame band (1.8–25 keV at a redshift of 1.5) at a high redshift. To distinguish the effect of a real X-ray absorption and the reflection component, X-ray spectroscopic observations for such broad-line AGNs below 0.7 keV in the observed frame are critical.

EDITOR: PLACE FIGURE 6 HERE.

To examine the correlation between the strength of optical broad-line and the X-ray absorption column density, we plotted the AGNs with redshift smaller than 0.75 in the $\text{H}\beta$ -to-[OIII] 5007Å versus hydrogen column density diagram in Figure 7. The narrow- or weak-broad-line AGNs with $\log N_{\text{H}}(\text{cm}^{-2}) = 22 \sim 23$ have 10 times smaller values of $\text{H}\beta$ /[OIII]5007Å than typical QSOs. The small ratio suggests existence of absorption with

A_V of larger than 2~3 mag to the broad-line region. The optical extinction corresponds to a hydrogen column density of $\log N_{\text{H}}(\text{cm}^{-2}) = 21.5 \sim 21.7$, according to the relation $N_{\text{H}}/A_V = 1.79 \times 10^{21} \text{ cm}^{-2} \text{ mag}^{-1}$, which is determined from observations of Galactic objects (e.g., Predehl & Schmitt 1995). Thus, the optical extinction derived from the $\text{H}\beta$ region is consistent with the X-ray spectra for these objects. One narrow-AGN and 5 weak-broad-line AGNs with $\log(\text{H}\beta/[\text{OIII}]5007\text{\AA})$ of less than 0 are fitted with smaller hydrogen column densities than $\log N_{\text{H}}(\text{cm}^{-2}) = 22$. In the $\text{H}\alpha$ region, however, 3/6 of them have a significant broad $\text{H}\alpha$ line and are plotted with open rectangles or an open star in Figure 7. They fall in the lower-right region in Figure 4. The small hydrogen column density is consistent with the existence of a broad $\text{H}\alpha$ line, which suggests smaller absorption to the broad-line region than AGNs with $\log N_{\text{H}}(\text{cm}^{-2}) = 22 \sim 23$. All strong-broad-line AGNs with $\log(\text{H}\beta/[\text{OIII}]5007\text{\AA})$ larger than 0 are fitted with hydrogen column density of less than $\log N_{\text{H}}(\text{cm}^{-2}) = 22$. These facts suggest the critical column density which divides the narrow-line and broad-line AGN is around $\log N_{\text{H}}(\text{cm}^{-2}) = 22$. The critical column density is consistent with the lower boundary of the distribution of absorbing column densities of Seyfert 2 galaxies (Risaliti, Maiolino, & Salvati 1999). Therefore, for AGNs with redshift smaller than 0.75, there is no broad-line AGN with a large absorption column density and the strengths of the broad Balmer lines are consistent with the hydrogen column density derived from the X-ray spectra.

EDITOR: PLACE FIGURE 7 HERE.

5. Number Counts and Contribution to the CXB

We hereafter divide the AGN sample at the intrinsic column density of $\log N_{\text{H}}(\text{cm}^{-2}) = 22$: we refer the AGNs with the column density larger and smaller than $\log N_{\text{H}}(\text{cm}^{-2}) = 22$

as “the absorbed AGN” and “the less-absorbed AGN”, respectively. At first, we include the four high-redshift broad-line AGNs fitted with the large column densities in the less-absorbed sample, because such large column densities could be only apparent (Section 4.2).

Figure 8 shows the cumulated logN-logS relations for the absorbed and for the less-absorbed samples in the SIS 3.5σ sample. Since the sensitivity limit is given in count rates, the actual flux limit depends on X-ray spectrum of sources. For an X-ray spectrum with the canonical photon index of type 1 AGNs ($\Gamma = 1.7$), the deepest source-detection limit of the SIS 3.5σ sample ($1.2 \text{ cts ksec}^{-1}$; see Table 1) is equivalent for $1.1 \times 10^{-13} \text{ erg cm}^{-2} \text{ s}^{-1}$ in the 2–10 keV band. If we assume an object with hydrogen column density of $\log N_{\text{H}}(\text{cm}^{-2}) = 23$ at redshift of 0.1, which corresponds to the hardest object in the LSS sample, the flux limit is estimated to be $1.6 \times 10^{-13} \text{ erg cm}^{-2} \text{ s}^{-1}$ in the 2–10 keV band. In the calculation of Figure 8, the SIS count rate was converted into the flux with the best-fit photon index determined in the 0.7–10 keV band for each source to take into account this effect. As noted from Figure 8, the surface number density of the absorbed AGNs is comparable to that of the less absorbed AGNs at flux larger than $2 \times 10^{-13} \text{ erg cm}^{-2} \text{ s}^{-1}$. The large fraction of the less-absorbed AGNs in the identified sample is due to different limiting flux for different X-ray spectra.

EDITOR: PLACE FIGURE 8 HERE.

At the first step, we estimate the contributions to the CXB, integrating the logN-logS relations from the brightest to the faintest object in each population of the LSS sample. For less-absorbed AGNs, absorbed AGNs, and clusters of galaxies, the summed fluxes of sources per unit area are $3.3 \times 10^{-12} \text{ erg cm}^{-2} \text{ s}^{-1} \text{ degree}^{-2}$, $6.3 \times 10^{-13} \text{ erg cm}^{-2} \text{ s}^{-1} \text{ degree}^{-2}$, and $1.4 \times 10^{-13} \text{ erg cm}^{-2} \text{ s}^{-1} \text{ degree}^{-2}$ and contributions to the CXB are 17%, 3%, and

0.7% , respectively, if we use the CXB flux determined in the LSS field (Ishisaki et al. 1999, 2.0×10^{-11} erg cm⁻² s⁻¹ degree⁻² in the 2–10 keV band).

As the second step, to determine contributions of each population in a wider flux range, we combined results of the *HEAO1* A2 sample (Piccinotti et al. 1982). The sample consists of 30 AGNs, 4 BL Lac objects, 30 clusters of galaxies, 1 starburst galaxy, and 3 unidentified sources with the flux limit of 3.1×10^{-11} erg cm⁻² s⁻¹ in the 2–10 keV band. In the 30 AGNs, 6 AGNs are fitted with hydrogen column density larger than $\log N_{\text{H}}(\text{cm}^{-2}) = 22$ (Schartel et al. 1997). The source number density at the flux limit is 2.4×10^{-3} degree⁻². If we assume that there is no break in the logN-logS relations, the slopes of the relations between the *HEAO1* A2 and the LSS limits can be determined. The results are shown in Table 5. In this flux range, the total number count in the 2–10 keV band has a slope (α of $N(> S) = kS^{-\alpha}$) of 1.5 and is consistent with that of smoothly distributed sources in a simple Euclidean geometry as reported in Ueda et al. (1998). However, the slope is a summation of steep slopes for AGNs and a shallow slope for clusters of galaxies. Thus the Euclidean distribution is an apparent effect. The slope of the logN-logS relation of clusters of galaxies in the flux range is consistent with that determined in the 0.5–2 keV band (1.15, Vikhlinin et al. 1998). Based on the slope of the logN-logS relation, the contributions from less-absorbed AGNs, absorbed AGNs, and clusters of galaxies are estimated to be 9%, 4%, and 1%, respectively, integrating the logN-logS relations from 3×10^{-11} erg cm⁻² s⁻¹ down to the flux limit of 2×10^{-13} erg cm⁻² s⁻¹ , which is the limit for absorbed AGNs and at which 16% of the CXB was resolved into discrete sources. The logN-logS relation of the absorbed AGNs with the four high-redshift broad-line AGNs is also shown in Figure 8 with a thin long-dashed line. Based on the logN-logS relation, the contribution of the absorbed AGNs with the four AGNs to the CXB is estimated to be 6%.

EDITOR: PLACE TABLE 5 HERE.

6. Redshift Distribution of Identified AGNs and Deficiency of Obscured QSO

To examine the redshift and luminosity distributions of the AGNs, we plot the X-ray luminosity versus redshift diagram of all the identified AGNs of the SIS 3.5σ sample in Figure 9a. Absorbed AGNs are marked with dots. At first, the high-redshift broad-line AGNs which are fitted with large column densities are included in the less-absorbed sample as in Section 5. The number ratio of absorbed AGNs-to-less-absorbed AGNs is clearly changing with redshift, luminosity, or both. If we limit the sample above the flux level of 2×10^{-13} erg cm $^{-2}$ s $^{-1}$, which is the flux limit for the absorbed AGNs, the redshift and luminosity distribution of the limited sample is also significantly different between these two populations. The number count of the absorbed AGNs is dominated by nearby low-luminous objects, in contrast to that of less-absorbed AGNs, which are dominated by QSOs at intermediate to high redshifts. In the same figure, the AGN sample from the *HEAO1* A2 survey (Piccinotti et al. 1982) is also plotted with small marks. Objects with hydrogen column density larger than $\log N_{\text{H}}(\text{cm}^{-2}) = 22$ are also marked with small dots (Schartel et al. 1997). The same tendency of deficiency of absorbed AGNs with a large luminosity is seen in their sample. Such a deficiency of luminous absorbed AGNs is also found in the *ROSAT*, *ASCA*, and *Beppo-SAX* deep surveys in the Lockman Hole (Hasinger et al. 1999). In Figure 9b, detection limits of the SIS 2–7 keV 3.5σ sample for intrinsic luminosities with various absorption column densities is shown as a function of redshift. In this calculation, we assume the intrinsic photon index of 1.7 and consider the response function of *ASCA* with the SIS. The difference between the survey limits of non-absorbed objects and that of objects with $\log N_{\text{H}}(\text{cm}^{-2}) = 22.5$ is less than 0.2 in the logarithmic-scale intrinsic luminosity at the redshift range from 0 to 1.5. Thus, we can detect objects with intrinsic column densities of up to $\log N_{\text{H}}(\text{cm}^{-2}) = 22.5$ at redshifts smaller than 1.5 in an unbiased fashion. At higher redshifts objects with column densities of up to $\log N_{\text{H}}(\text{cm}^{-2}) = 23$ are detected without bias, thanks to the redshift effect. It

should be noted that the peak of the distribution of absorption column densities of type 2 Seyferts in the nearby universe ($\log N_{\text{H}}(\text{cm}^{-2}) > 23$; Risaliti et al. 1999) is beyond the detection limit.

EDITOR: PLACE FIGURE 9 HERE.

To examine the deficiency of luminous absorbed AGNs more quantitatively, we compare the redshift distribution of absorbed AGNs and that of less-absorbed AGNs, considering the difference of their X-ray spectra. In Figure 10a, we show the redshift distribution of less-absorbed AGNs as well as the expected redshift distribution of broad-line AGNs. The four high-redshift broad-line AGNs which are fitted with large column densities are included in the less-absorbed sample. The expected redshift distribution of broad-line AGNs is calculated based on a hard-band X-ray luminosity function of broad-line AGNs and its evolution (Boyle et al. 1998a); they are determined by an AGN sample from *ASCA* observations of Deep *ROSAT* fields and optical identifications of the Large Area Sky Survey/Modulation Collimator catalog obtained from *HEAO1* mission. The expected redshift distribution matches well to that of the LSS sample. Based on Kolmogorov-Smirnov test, the probability that the observed redshift distribution agrees with the model is calculated to be 64%. Thus, we use the hard-band X-ray luminosity function as a base model for less-absorbed AGNs. In Figure 10b, we compare the redshift distribution of absorbed AGNs in the LSS sample with the expected distribution of them calculated by assuming that the shape of the intrinsic (which means absorption corrected) luminosity function of absorbed AGNs is the same as that of less-absorbed AGNs. The equal number density of AGNs with $\log N_{\text{H}}(\text{cm}^{-2}) = 22 \sim 23$ to that of less-absorbed AGN is the same as in the spectrum model of the CXB; e.g., Comastri et al. (1995) used the value of 1.23 for the number ratio of AGNs with absorption of $\log N_{\text{H}}(\text{cm}^{-2}) = 22 \sim 23$ to those with absorption less than $\log N_{\text{H}}(\text{cm}^{-2}) = 22$. As seen in Figure 10b, at redshift smaller than

0.4, in which the X-ray luminosity of the sample AGN is less than 10^{44} erg s⁻¹, the number of absorbed AGNs is comparable to the expectation. However, at redshifts larger than 0.4, the total expected number is about 10, which contrasts to the non-detection. The observed redshift distribution is different from the model redshift distribution; Kolmogorov-Smirnov test gives a probability of only 5% for the null hypothesis that the redshift distribution of absorbed AGNs is the same as the model, thus the hypothesis is rejected. Therefore, our sample suggests the deficiency of the absorbed AGNs with the column density of $\log N_{\text{H}}(\text{cm}^{-2}) = 22 \sim 23$, in the redshift range between 0.5 and 2.0, or in the X-ray luminosity range larger than 10^{44} erg s⁻¹, or both. We plot the redshift distribution of the four high-redshift broad-line AGNs with hard X-ray spectra in Figure 10b with a histogram shaded with dashed lines. By including the four AGNs, the observed redshift distribution agrees the model redshift distribution with probability of 60%. If their large column densities are real, they could complement the deficiency of absorbed high-redshift luminous AGNs. Revealing the column density distribution of absorbed AGN as a function of redshift and luminosity and constructing the model of the origin of the CXB more accurately will be an important objective for the next generation X-ray surveys.

EDITOR: PLACE FIGURE 10 HERE.

7. Properties of identified AGNs in other wavelengths

7.1. Optical Photometric Properties

We have examined the optical appearance of each identified object. The results are indicated in the last column of the Table 4. All of the low-luminosity AGNs show their host galaxy component in the optical light. We calculate optical total absolute

magnitudes of the identified objects, using $\alpha = -0.5$, which corresponds to $V - R$ of 0.22 mag. The results are shown in Table 4 and plotted in Figure 11 as a function of X-ray luminosity. For high-luminosity AGNs, hard X-ray luminosities correlate well with optical luminosities. On the other hand, for the low-luminosity AGNs whose optical light is affected and maybe dominated by their host galaxy components, the correlation is broken. Considering the break, we estimate the absolute magnitudes of the host galaxies to be around $M_V = -21 \sim -23.5$ mag and are similar to that of QSO host galaxies (Bahcall et al. 1997).

EDITOR: PLACE FIGURE 11 HERE.

The optical colors of luminous broad-line AGNs distribute from $B - R$ of -0.2 mag to 1.1 mag, consistent with the expected color range for broad-line AGNs. There is no broad-line QSO which has a $B - R$ color larger than 2.0 mag, which is a criterion for *red* QSOs in Kim & Elvis (1999). Two low-luminosity broad-line AGNs (AX J131725+3300(192) and AX J131407+3158(127)) which show a broad $H\alpha$ emission have red optical colors. The red colors are probably affected by the host galaxy, because their optical images show the host galaxy components.

7.2. Radio and Far-infrared Properties

To examine radio properties of the identified AGNs, we show a radio versus hard X-ray luminosity diagram in Figure 12. There are two sequences in the diagram; three objects which have large radio-to-hard X-ray luminosity ratios correspond to radio-loud AGNs and others which have smaller ratios correspond to radio-quiet AGNs. The radio-to-hard X-ray ratios of the radio-loud sequence are consistent with the average SED of radio-loud QSO (Elvis et al. 1994). On the other hand, the radio-quiet sequence has one order of

magnitude larger radio-to-hard X-ray luminosity ratio than the average SED of radio-quiet QSO (Elvis et al. 1994). Based on the dispersion of the radio-to-optical luminosity ratios of radio-quiet QSOs (Visnovsky et al. 1992), the large radio-to-hard X-ray luminosity ratio is accounted by a scatter and a selection bias for radio louder objects. The fraction (3/30) of radio-loud AGNs in the total AGN sample is consistent with that in the low-luminosity sample of optically selected QSOs (13%) (Visnovsky et al. 1992). In radio images, all radio-quiet AGNs show only one point-like component. Two radio-loud AGNs consist of two components; one dominates the total flux located on the optical position and the other fainter source is ~ 15 arcsec away from the central component.

EDITOR: PLACE FIGURE 12 HERE.

In the LSS sample, only the galactic star is detected in the *IRAS* survey (Moshir et al. 1992). None of the AGN is detected in the *IRAS* Faint Source Survey. Based on the flux limit of the *IRAS* survey in the LSS region (0.1 Jy in 60 μm), most of the AGNs have lower limits to the logarithmic ratio of 2–10 keV luminosity-to-far-infrared luminosity ($\nu_{60\mu\text{m}}L\nu_{60\mu\text{m}}$) of less than -1 , consistent with those known for QSOs (-1) and only one object (AX J131822+3347 (235)) has a lower limit (-0.6) to the logarithmic ratio larger than the typical value of QSOs. The lower limits to the logarithmic ratio are significantly larger than those of star-forming galaxies, which have logarithmic ratios around -4 .

8. Summary

We present results of optical identifications of the X-ray sources detected in the *ASCA* Large Sky Survey. Optical spectroscopic observations were done for 34 X-ray sources which were detected with the SIS in the 2–7 keV band above 3.5σ . The flux limit corresponds to

$\sim 1 \times 10^{-13}$ erg cm $^{-2}$ s $^{-1}$ in the 2–10 keV band. The sources are identified with 30 AGNs, 2 clusters of galaxies, and 1 galactic star. Only 1 source is still unidentified.

All of the X-ray sources that have a hard X-ray spectrum with an apparent photon index of smaller than 1 in the 0.7–10 keV band are identified with narrow-line or weak-broad-line AGNs at redshifts smaller than 0.5. This fact supports the idea that absorbed X-ray spectra of narrow-line and weak-broad-line AGNs make the Cosmic X-ray Background (CXB) spectrum harder in the hard X-ray band than that of a broad-line AGN, which is the main contributor in the soft X-ray band. Assuming their intrinsic spectra are same as a broad-line AGN (a power-law model with a photon index of 1.7), their X-ray spectra are fitted with hydrogen column densities of $\log N_{\text{H}}(\text{cm}^{-2}) = 22 \sim 23$ at the object's redshift. On the other hand, X-ray spectra of the other AGNs are consistent with that of a nearby type 1 Seyfert. In the sample, four high-redshift luminous broad-line AGNs show a hard X-ray spectrum with an apparent photon index of 1.3 ± 0.3 . The hardness may be explained by the reflection component of a type 1 Seyfert. The hard X-ray spectra may also be explained by absorption with $\log N_{\text{H}}(\text{cm}^{-2}) = 22 \sim 23$ at the object's redshift, if we assume an intrinsic photon index of 1.7. The origin of the hardness is not clear yet.

Based on the logN-logS relations of each population, contributions to the CXB in the 2–10 keV band are estimated to be 9% for less-absorbed AGNs ($\log N_{\text{H}}(\text{cm}^{-2}) < 22$) including the four high-redshift broad-line AGNs with a hard X-ray spectrum, 4% for absorbed AGNs ($22 < \log N_{\text{H}}(\text{cm}^{-2}) < 23$, without the four hard broad-line AGNs), and 1% for clusters of galaxies in the flux range from 3×10^{-11} erg cm $^{-2}$ s $^{-1}$ to 2×10^{-13} erg cm $^{-2}$ s $^{-1}$. If the four hard broad-line AGNs are included in the absorbed AGNs, the contribution of the absorbed AGNs to the CXB is estimated to be 6%.

In optical spectra, there is no high-redshift luminous cousin of a narrow-line AGN in our sample. The redshift distribution of the absorbed AGNs are limited below $z = 0.5$

excluding the four hard broad-line AGNs, in contrast to the existence of 15 less-absorbed AGNs above $z = 0.5$. The redshift distribution of the absorbed AGNs suggests a deficiency of AGNs with column densities of $\log N_{\text{H}}(\text{cm}^{-2}) = 22$ to 23 in the redshift range between 0.5 and 2, or in the X-ray luminosity range larger than 10^{44} erg s $^{-1}$, or both. If the large column densities of the four hard broad-line AGNs are real, they could complement the deficiency of X-ray absorbed luminous high-redshift AGNs.

MA, KO, and TY would like to thank S.Okamura, M.Sekiguchi and the MOSAIC CCD camera team, and staff members of the KISO observatory for their support during the imaging observations. MA, KO, and TY appreciate the support from members of the University of Hawaii observatory during the spectroscopic observations. KO is grateful to the hospitality during his stay at the Institute for Astronomy, University of Hawaii, where a part of this work was done. MA, KO, YU, and IL wish to thank members of the Calar Alto observatory for their help during the spectroscopic observations. We are also grateful to the referee for his useful suggestions. This research has made use of NASA/IPAC Extragalactic Database (NED), which is operated by the Jet Propulsion Laboratory, Caltech, under contract with the National Aeronautics and Space Administration. MA, WK, and MS acknowledge support from a Research Fellowships of the Japan Society for the Promotion of Science for Young Scientists. The optical follow-up program is supported by grants-in-aid from the Ministry of Education, Science, Sports and Culture of Japan (06640351, 08740171, 09740173) and from the Sumitomo Foundation.

A. *ROSAT* HRI Data Reduction and Source Detection

ROSAT HRI observations were made in 2 fields with a 20 ksec exposure in December 1997. These fields were centered at $\alpha=13^{\text{h}}14^{\text{m}}36^{\text{s}}$, $\delta=32^{\circ}01'12''$ (LSS-HRI1) and $\alpha=13^{\text{h}}12^{\text{m}}29^{\text{s}}$,

$\delta=31^{\circ}13'12''$ (LSS-HRI2) (J2000) with a radius of $19'$.

These data were reduced with EXSAS package (Zimmermann et al. 1994) on the MIDAS. For the source detection, we applied the **detect** command selecting photons in the PHA channel range from 2 to 8, only. X-ray sources detected in the HRI follow-up observations with Maximum Likelihood larger than 10 were listed in Table 6.

The conversion factor from a count rate to a 0.5–2.0 keV flux is 1.854×10^{-14} erg cm $^{-2}$ s $^{-1}$ cts $^{-1}$ ksec. Thus the flux of the faintest source corresponds to 1.13×10^{-14} erg cm $^{-2}$ s $^{-1}$. Considering systematic shifts between candidates of optical counterparts and X-ray sources, we shifted the X-ray positions with $\Delta\alpha = -3.''39$, $\Delta\delta = +5.''08$ and $\Delta\alpha = -2.''37$, $\Delta\delta = +3.''18$ for regions LSS-HRI1 and LSS-HRI2, respectively.

EDITOR: PLACE TABLE 6 HERE.

B. Cross identification with the *ROSAT* PSPC catalogs and the VLA FIRST catalog

We summarize the identifications of the *ASCA* LSS sources with the *ROSAT* PSPC sources and the VLA FIRST radio sources in Table 7.

EDITOR: PLACE TABLE 7 HERE.

REFERENCES

- Abell, G.O., Corwin, H.G., & Olowin, R.P. 1989, *ApJS*, 70, 1
- Akiyama, M., et al. 1998a, *ApJ*, 500, 173
- Akiyama, M., et al. 1998b, *AN*, 319, 63
- Almaini, O., Boyle, B.J., Griffiths, R.E., Shanks, T., Stewart, G.C., Georgantopoulos, I.
1995, *MNRAS*, 277, L31
- Bade, N., et al. 1998, *A&AS*, 127, 145
- Bahcall, J.N., Kirhakos, S., Saxe, D.H., & Schneider, D.P. 1997, *ApJ*, 479, 642
- Barcons, X., Franceschini, A., De Zotti, G., Danese, L., & Miyaji, T. 1995, *ApJ*, 455, 480
- Barcons, X., Carballo, R., Ceballos, M.T., Warwick, R.S., & Gonzalez-Serrano, J.I. 1998,
MNRAS, 301, L25
- Becker, R. H., White, R. L., & Helfand, D. J. 1995, *ApJ*, 450, 559
- Boyle, B.J., Staveley-smith, L., Stewart, G.C., Georgantopoulos, I., Shanks, T., & Griffiths,
R.E. 1993, *MNRAS*, 265, 501
- Boyle, B.J., Georgantopoulos, I., Blair, A.J., Stewart, G.C., Griffiths, R.E., Shanks, T.,
Gunn, K.F., & Almaini, O. 1998a, *MNRAS*, 296, 1
- Boyle, B.J., Georgantopoulos, I., Blair, A.J., Stewart, G.C., Griffiths, R.E., Shanks, T.,
Gunn, K.G., & Almaini, O. 1998b, *MNRAS*, 297, 53
- Comastri, A., Setti, G., Zamorani, G., & Hasinger, G. 1995, *A&A*, 296, 1
- De Ruiter H.R., Zamorani G., Parma P., Hasinger G., Hartner G., Trümper J., Burg R.,
Giacconi R., & Schmidt M., 1997, *A&A*, 319, 7

- Elvis, M., et al. 1994, ApJS, 95, 1
- Evans, D.W. 1989, A&AS, 78, 249
- Falco, E.E., Kochanek, C.S., & Munoz, J.A., 1998, ApJ, 494, 47
- Fiore, F., et al. 1999, MNRAS, 306, L55
- Francis, P.J., Hewett, P.C., Foltz, C.B., Chaffee, F.H., Weymann, R.J., & Morris, S.L. 1991, ApJ, 373, 465
- Gendreau, K. C., et al. 1995, PASJ, 47, L5
- Georgantopoulos, I., Stewart, G.C., Blair, A.J., Shanks, T., Griffiths, R.E., Boyle, B.J., Almaini, O., & Roche, N. 1997, MNRAS, 291, 203
- Giacconi, R., Gursky, H., Paolini, F.R., & Rossi, B.B. 1962, Phys. Rev. Lett., 9, 439
- Gondek, D., Zdziarski, A.A., Johnson, W.N., George, I.M., McNaron-Brown, K., Magdziarz, P., Smith, D., & Gruber, D.E. 1996, MNRAS, 282, 646
- Hasinger, G., Burg, R., Giacconi, R., Schmidt, M., Trümper, J., & Zamorani, G. 1998, A&A, 329, 482
- Hasinger, G., Lehmann, I., Giacconi, R., Schmidt, M., Trümper, J., & Zamorani, G. 1999, in Proc ‘Highlights in X-ray Astronomy’, astro-ph/9901103
- Hartwick, F.D.A., & Schade, D. 1990, ARA&A, 28, 437
- Inoue, H., Kii, T., Ogasaka, Y., Takahashi, T., Ueda, Y. 1996, in Proc ‘Röntgenstrahlung from the Universe’, eds. Zimmermann, H.U., Trümper, J., and Yorke, H. MPE Report 263, 323

- Ishisaki, Y., Makishima, K., Takahashi, T., Ueda, Y., Ogasaka, Y., & Inoue, H. 1999, ApJ, submitted
- Kim, D., & Elvis, M. 1999, ApJ, 516, 9
- Kotilainen J.K., Ward, M.J., Boisson, C., et al. 1992, MNRAS, 256, 125
- Lawrence, A. 1991, MNRAS, 252, 586
- Madau, P., Ghisellini, G., & Fabian, A.C. 1994, MNRAS, 270, L17
- McMahon, R.G., Irwin, M.J., & Hazard, C. 1992, Gemini Issue, 36, 1
- Moshir, M., et al. 1992, Explanatory Supplement to the IRAS Faint Source Survey, Version 2, JPL D-10015 8/92 (Pasadena: JPL)
- Moreau, O., & Reboul, H. 1995, A&AS, 111, 169
- Ohta, K., Yamada, T., Nakanishi, K., Ogasaka, Y., Kii, T., & Hayashida, K. 1996, ApJ, 458, L57
- Osterbrock, D. E. 1989, Astrophysics of Gaseous Nebulae and Active Galactic Nuclei, University Science Books
- Piccinotti, G., Mushotzky, R. F., Boldt, E. A., Holt, S. S., Marshall, F. E., Serlemitsos, P. J., & Shafer, R.A. 1982, ApJ, 253, 485
- Predehl, P., & Schmitt, J.H.M.M. 1995, A&A293, 889
- Richstone, D.O., & Schmidt, M. 1980, ApJ, 235, 361
- Risaliti, G., Maiolino, R., & Salvati, M. 1999, ApJ, 522, 157
- Sakano, M., et al. 1998, ApJ, 505, 129

- Sakano, M., et al. 1999, *Advances in Space Research*, in press
- Schartel, N., Schmidt, M., Fink, H.H., Hasinger, G., & Trümper, J. 1997, *A&A*, 320, 696
- Schmidt, M., et al. 1998, *A&A*, 329, 495
- Sekiguchi, M., Iwashita, H., Doi, M., Kashikawa, N., & Okamura, S. 1992, *PASP*, 104, 744
- Schade, D. 1991, *AJ*, 102, 869
- Stocke, J.T., Liebert, J., Maccacaro, T., Griffiths, R.E., & Steiner, J.E. 1982, *ApJ*, 252, 69
- Stocke, J.T., Morris, S.L., Gioia, I.M., Maccacaro, T., Schild, R., Wolter, A., Fleming, T.A., & Henry, J.P. 1991, *ApJS*, 76, 813
- Takase, B., & Miyauchi-Isobe, N. 1986, *Annals of the Tokyo Ast. Obs.*, 21, 181
- Turner, T. J., & Pounds, K. A. 1989, *MNRAS*, 240, 833
- Ueda, Y. 1996, PhD. thesis, University of Tokyo
- Ueda, Y., et al. 1998, *Nature*, 391, 866
- Ueda, Y., et al. 1999a, *ApJ*, 518, 656 (Paper I)
- Ueda, Y., et al. 1999b, *Advances in Space Research*, in press
- Usher, P.D. 1981, *ApJS*, 46, 117
- Visnovsky, K.L., Impey, C.D., Foltz, C.B., Hewett, P.C., Weymann, R.J., & Morris, S.L. 1992, *ApJ*, 391, 560
- Vikhlinin, A., Mcnamara, B.R., Forman, W., Jones, C., Quintana, H., & Hornstrup, A. 1998, *ApJ*, 502, 558
- Voges, W., et al. 1999, *A&A*, 349, 389

Webster, R., et al. 1995, *Nature*, 375, 469

Wills, D., & Wills, B.J. 1976, *ApJS*, 31, 143

Winkler, H. 1992, *MNRAS*, 257, 677

Zimmermann, H.U., Becker, W., Belloni, T., et al. 1994, *MPEreport*, 257

Zwicky, F., Herzog, E., & Wild, P. 1961, *Catalogue of Galaxies and of Clusters of Galaxies*,
(Carnegie Institution of Washington)

Fig. 1.— Optical finding charts and spectra of identified objects. The field of view of the finding charts is $1'.6 \times 1'.6$. Large circles have a radius of $0'.6$ and correspond to the 90% confidence error circles of ASCA sources. Middle and small size circles have radii of $20''$ and $5''$ and correspond to error circles of *ROSAT* PSPC and HRI sources, respectively. Positions of FIRST radio sources are indicated by small rectangles. Objects which have an UV-excess or a blue $B - R$ colors are marked with pentagons. The objects listed in Table 2 are labeled with “A”, “B”, “C”, and “Z”. The spectrum of each identified object is shown with the identification label and classification. Positions of atmospheric absorption lines are shown as a cross with a circle.

Fig. 2.— The distribution of the identified objects within the X-ray error circles. Open circles, crosses, and an asterisk represent AGNs, clusters of galaxies, and a galactic star, respectively. Inner and outer circles have radii of $0'.6$ and $0'.8$. The inner circle corresponds to the estimated error radius of the LSS X-ray sources in the 90% confidence level.

Fig. 3.— 2–10 keV flux versus optical R band magnitude diagram of the identified objects. Marks are the same as in Figure 2. The upper limit of the optical magnitude of AX J131832+3259(199) is indicated with a plus sign with an upward arrow. Dashed lines represent X-ray-to-optical flux ratio of $\log f_X/f_V = +2, +1, 0, -1, -2, -3,$ and -4 from top to bottom.

Fig. 4.— The distribution of identified AGNs in the $\log(\text{H}\alpha/[\text{NII}]6583\text{\AA})$ versus $\log(\text{H}\beta/[\text{OIII}]5007\text{\AA})$ diagram. Equivalent widths for Balmer lines include both broad and narrow emission lines. Objects which were not observed in the $\text{H}\alpha$ region are plotted in the right box. Upper limits are indicated with downward arrows. AGNs which have a hard X-ray spectrum (an apparent photon index smaller than 1) are indicated with dots.

Fig. 5.— Apparent photon index (0.7–10 keV) versus redshift diagram of the identified objects. Marks are the same as in Figure 2. Horizontal solid line shows the photon index of the CXB. Expected apparent photon index for a type 1 Seyfert in the observed 0.7–10 keV band is shown with a dashed line as a function of redshifts. See Section 4.

Fig. 6.— Fitted column density versus 2–10 keV luminosity diagram of the identified AGNs. The X-ray luminosities are not corrected for the absorption. AGNs with a hard X-ray spectrum which have an apparent photon index smaller than 1 are indicated with dots. Upper limits for column densities are indicated with downward arrows.

Fig. 7.— Fitted column density versus $\log(H\beta / [OIII] 5007\text{\AA})$ of the identified AGNs. An AGN which shows a broad $H\alpha$ and a broad $H\beta$ lines is shown with an open star, AGNs with a broad $H\alpha$ and no significant broad $H\beta$ line are plotted with open rectangles, and AGNs without significant broad $H\alpha$ nor $H\beta$ are indicated with filled rectangles. Note these AGNs are observed in both $H\alpha$ and $H\beta$ regions. AGNs which are observed only in the $H\beta$ region are plotted with open triangles for objects with a broad $H\beta$ line, and with filled triangles for objects without broad $H\beta$ line. Upper limits are indicated with downward and leftward arrows.

Fig. 8.— Cumulative logN-logS relations in the 2–10 keV band for the SIS 2–7 keV 3.5σ sample. The thin solid line, the thick dotted line, the thick long-dashed line, and the thin long-dashed line correspond to the logN-logS relations for all sources, the less-absorbed ($\log N_H(\text{cm}^{-2}) < 22$) AGNs, the absorbed ($\log N_H(\text{cm}^{-2}) > 22$ without the 4 hard broad-line AGNs) AGNs, and the absorbed ($\log N_H(\text{cm}^{-2}) > 22$ with the 4 hard broad-line AGNs) AGNs, respectively. The short dashed line indicates the logN-logS relations of clusters of galaxies, and the dot dashed line shows that of an unidentified source. The thick solid line represents extrapolation with a slope of -1.5 from the *HEAO1* A2 results. Survey limits for less-absorbed AGNs and clusters of galaxies are $1 \times 10^{-13} \text{ erg cm}^{-2} \text{ s}^{-1}$, whereas it is

1.6×10^{-13} erg cm $^{-2}$ s $^{-1}$ for absorbed AGNs with the hardest X-ray spectrum (see Section 5).

Fig. 9.— a) 2–10 keV luminosity versus redshift diagram of the identified sample. The LSS AGNs are plotted with large open circles. Absorbed ($\log N_{\text{H}}(\text{cm}^{-2}) > 22$) AGNs are marked with dots. The solid line is the detection limit of the SIS 2–7 keV 3.5σ sample for non-absorbed AGN. We also plot the *HEAO1* A2 sample of AGNs (Piccinotti et al. 1982) with small marks. b) Detection limit of the SIS 2–7 keV 3.5σ sample to an *intrinsic* 2–10 keV luminosity as a function of redshift. From top to bottom, column densities of $\log N_{\text{H}}(\text{cm}^{-2}) = 24.0, 23.5, 23.0, 22.5, 22.0, 21.5, 21.0$, and no absorption with an intrinsic photon index of 1.7 are assumed. The survey limit of the SIS 3.5σ sample is 1.2 cts ksec $^{-1}$ in the 2–7 keV band.

Fig. 10.— a) Comparison of redshift distribution of the less-absorbed ($\log N_{\text{H}}(\text{cm}^{-2}) < 22$) AGNs in the LSS sample with that expected from a broad-line AGN luminosity function in the hard X-ray band. The shaded histogram is the redshift distribution of the LSS AGN sample and the solid line is the expected redshift distribution. The four high redshift broad line AGNs with a hard X-ray spectrum are included in this histogram. See Section 6. b) Comparison of redshift distribution of the absorbed ($\log N_{\text{H}}(\text{cm}^{-2}) > 22$) AGNs in the LSS sample with that expected from a broad-line AGN luminosity function in the hard X-ray band with an absorption of $\log N_{\text{H}}(\text{cm}^{-2}) = 22.5$. The shaded histogram is the redshift distribution of the absorbed AGNs and the histogram shaded with dashed lines is that of the broad-line AGNs with a hard X-ray spectrum mentioned above. The solid line is the expected redshift distribution. The black histogram at the right-top corner refers to unidentified source.

Fig. 11.— Hard X-ray luminosity versus optical *V* band absolute magnitude diagram of the identified AGNs.

Fig. 12.— Hard X-ray luminosity versus radio 1.4 GHz luminosity diagram of the identified AGNs. Downward arrows show upper limit on the radio luminosities.

Count Rate	Area
(cts ksec ⁻¹)	(degree ²)
1.2	0.5
1.4	1.0
1.6	2.0
2.0	3.0
3.0	4.8
4.0	5.0
6.0	5.5
10.0	5.7
20.0	5.8

Table 1: Survey Area as a function of the SIS 2–7 keV count rate for the 3.5σ sample from Paper I.

	log N(>S) ^b		α^c	Contributions ^d
	<i>HEAO1</i> A2	<i>ASCA</i> LSS		
Flux limit ^a	3×10^{-11}	2×10^{-13}		2×10^{-13}
Total	–2.62	$0.80^{+0.07}_{-0.08}$	$1.55^{+0.03}_{-0.05}$	16%
less-absorbed AGN	–2.66	$0.47^{+0.08}_{-0.10}$	$1.42^{+0.04}_{-0.05}$	9%
absorbed AGN (without 4 broad-line AGN)	–3.68	$0.28^{+0.16}_{-0.25}$	$1.80^{+0.07}_{-0.11}$	4%
absorbed AGN (with 4 broad-line AGN)	–3.68	$0.44^{+0.13}_{-0.19}$	$1.89^{+0.06}_{-0.09}$	6%
Cluster	–2.98	$-0.74^{+0.23}_{-0.52}$	$1.02^{+0.11}_{-0.24}$	1%

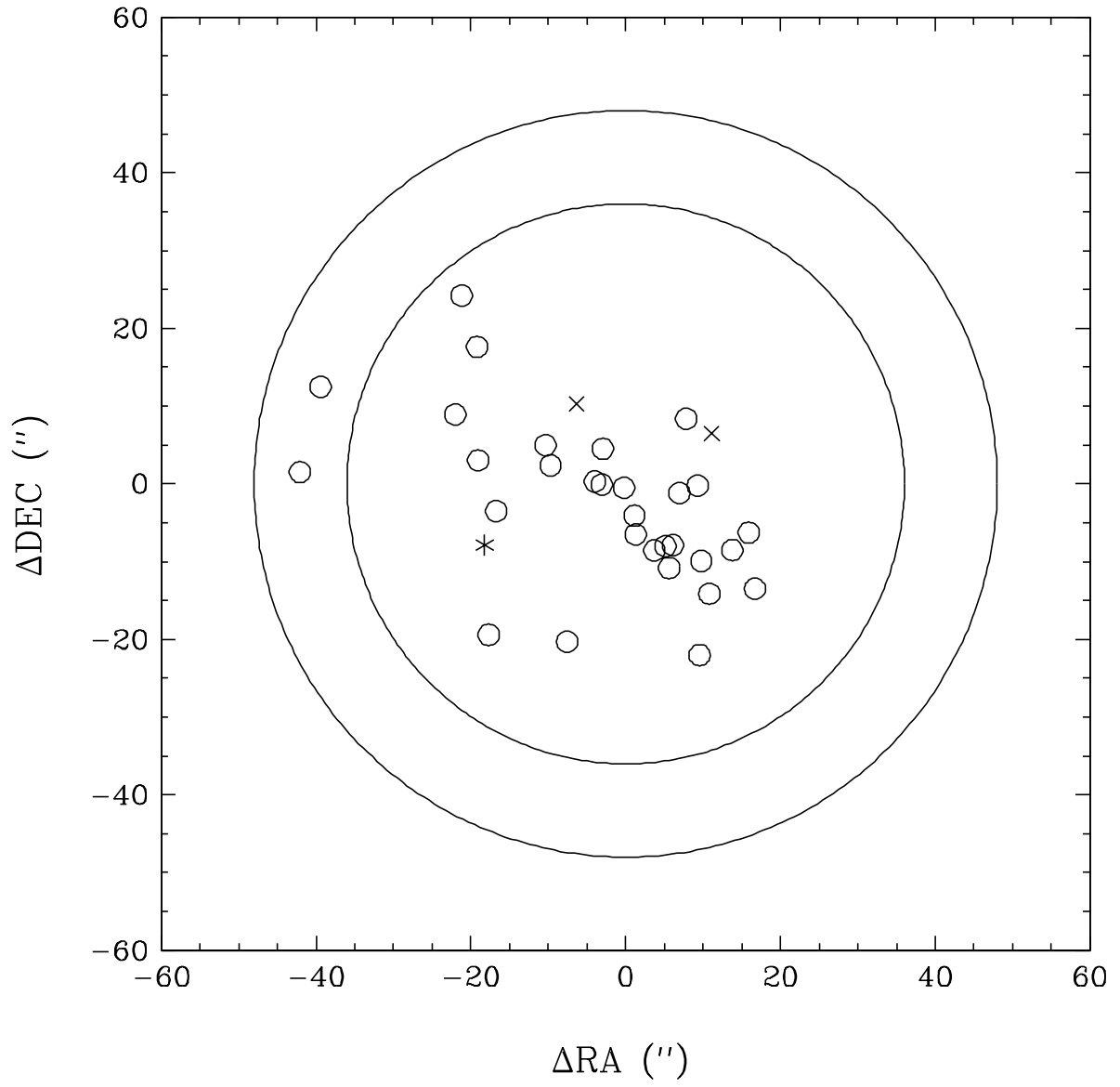
Table 5: LogN-logS relations of various populations and their contributions to the CXB in the 2–10 keV band.

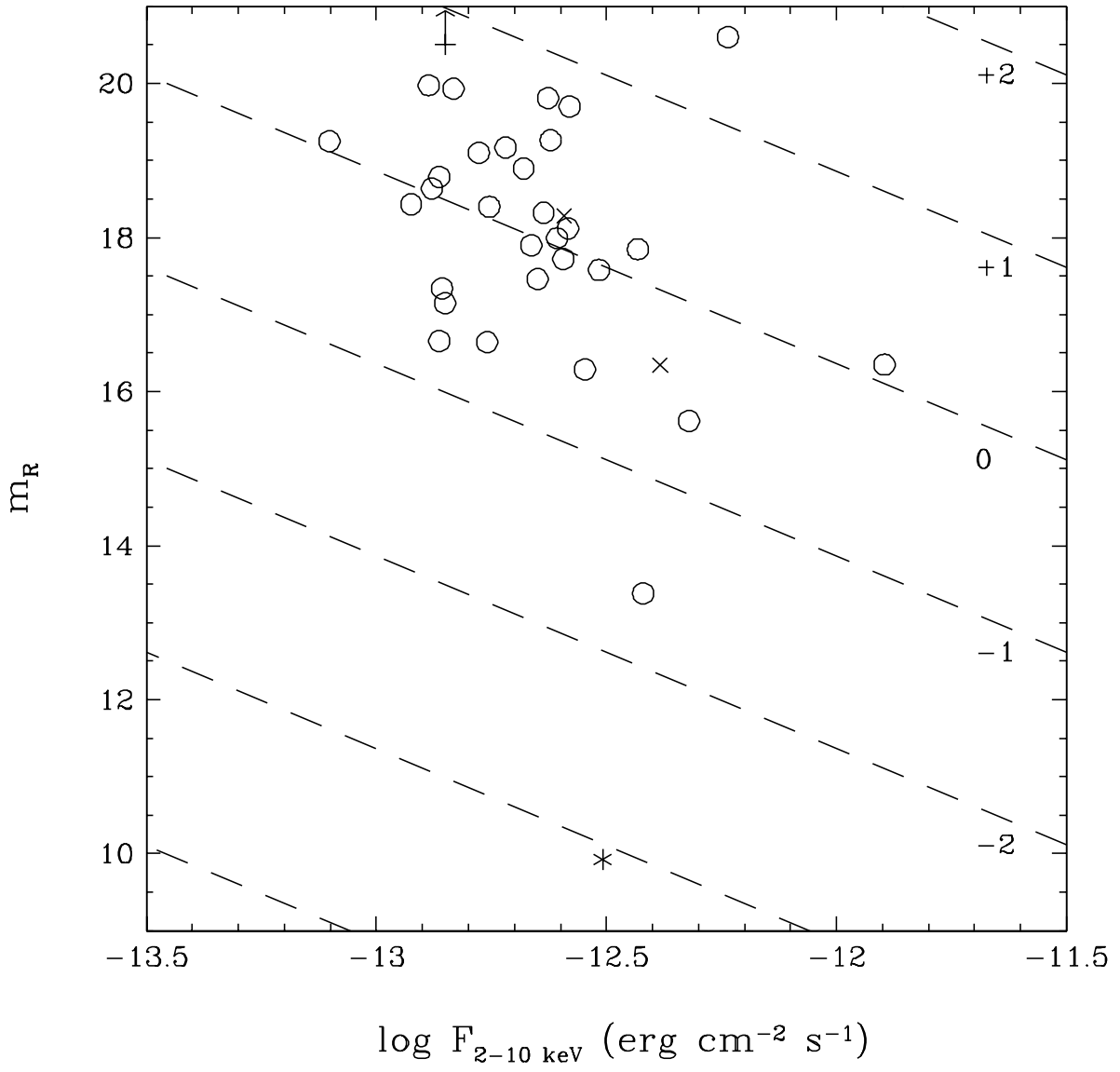
^aFlux limit in unit of $\text{erg cm}^{-2} \text{s}^{-1}$ in the 2–10 keV band.

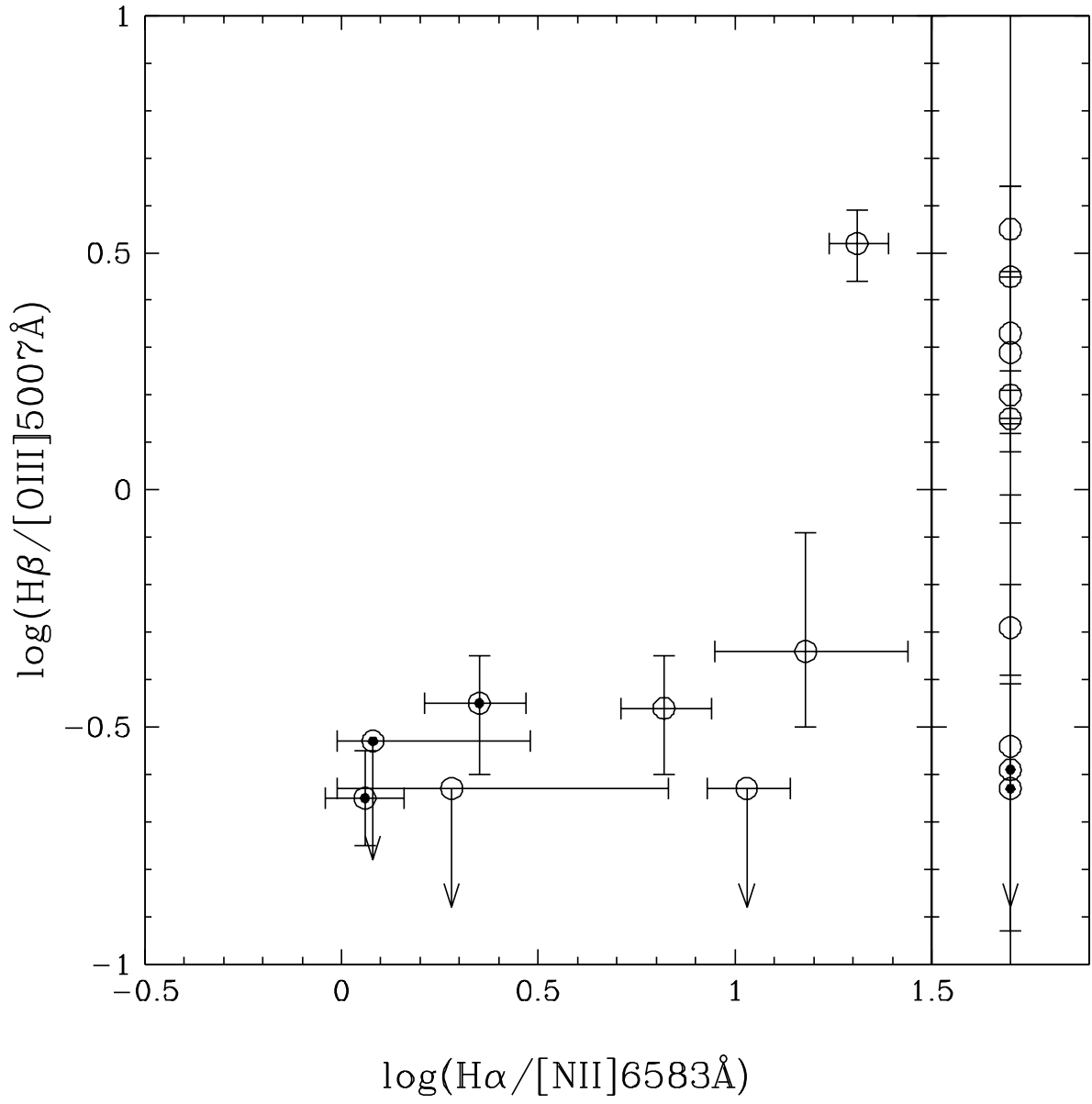
^bSource number densities at the flux limits in degree^{-2} . The errors of the LSS source number densities are estimated with the square root of the detected number.

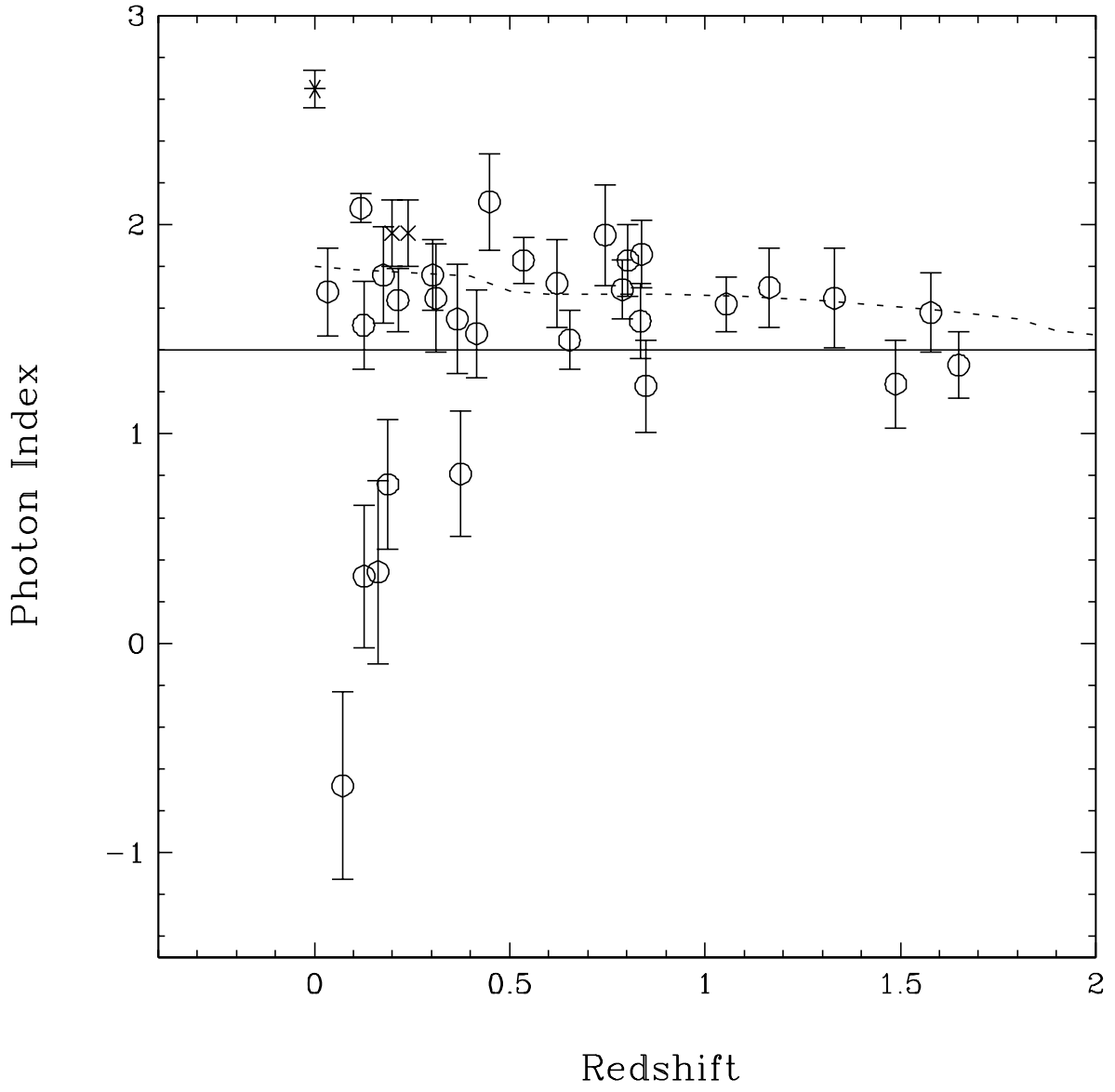
^cSlopes of logN-logS relations in the flux range.

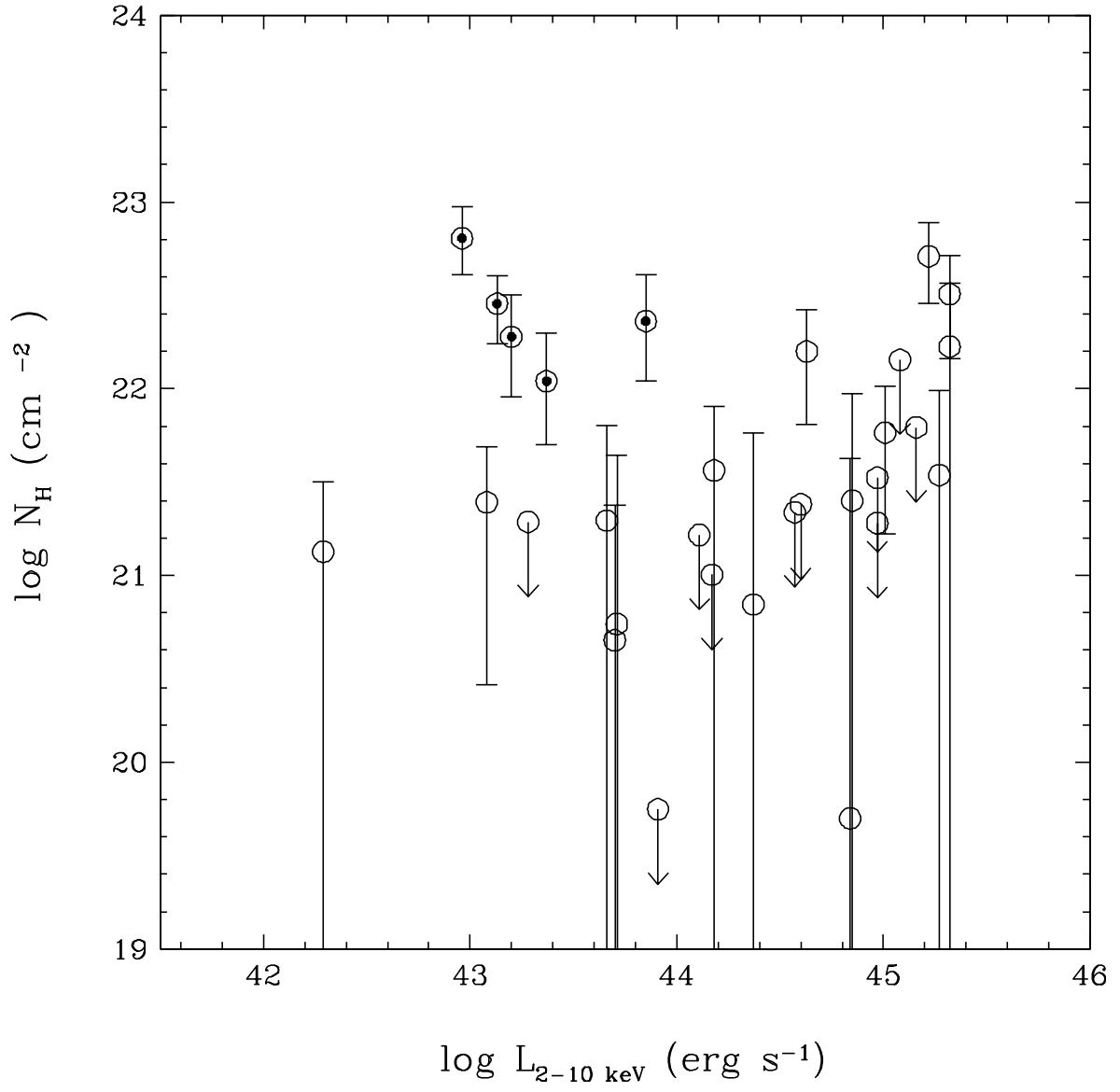
^dContributions to the CXB from the sources in the flux range from $3 \times 10^{-11} \text{ erg cm}^{-2} \text{ s}^{-1}$ to the flux limits.

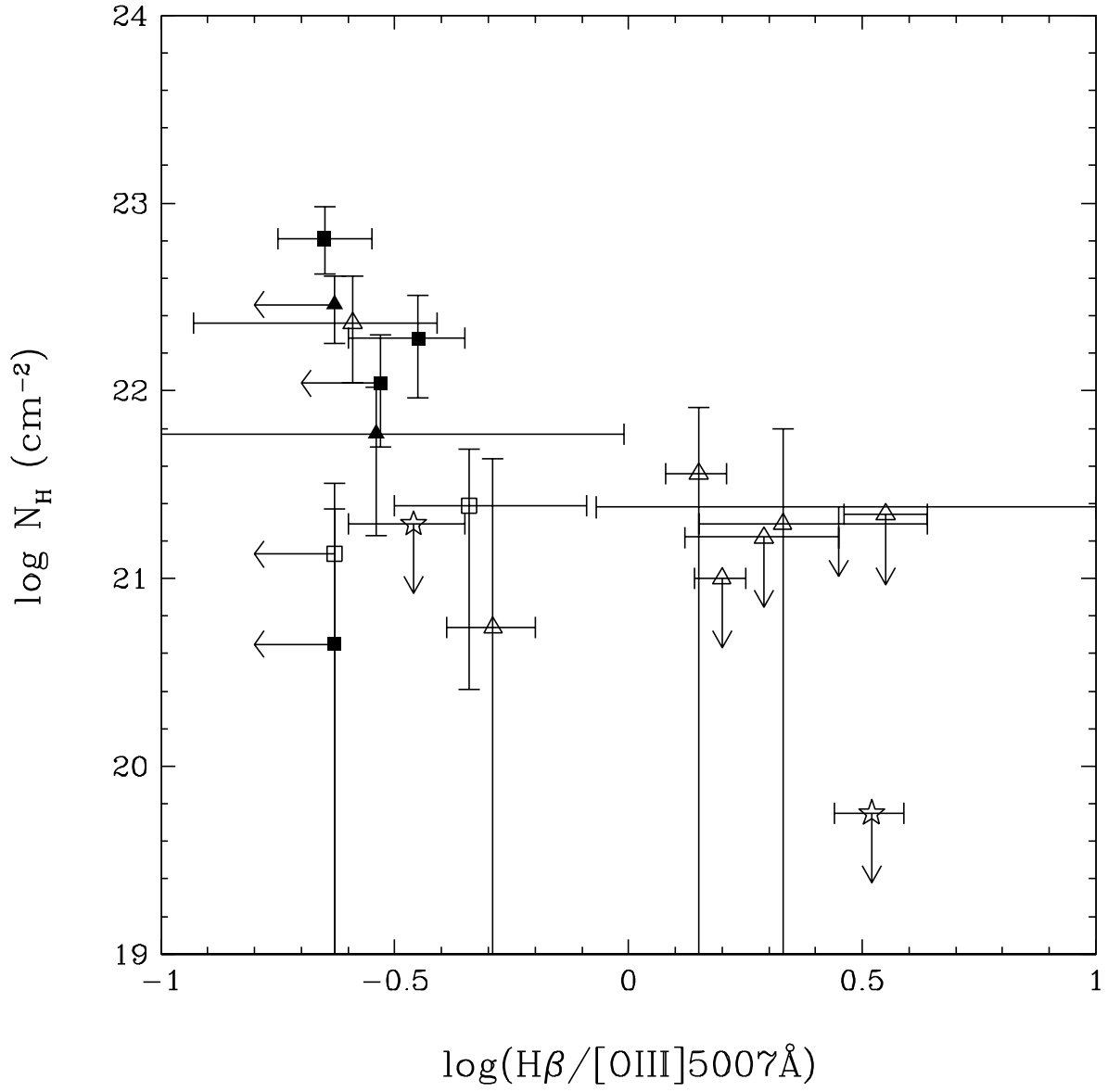


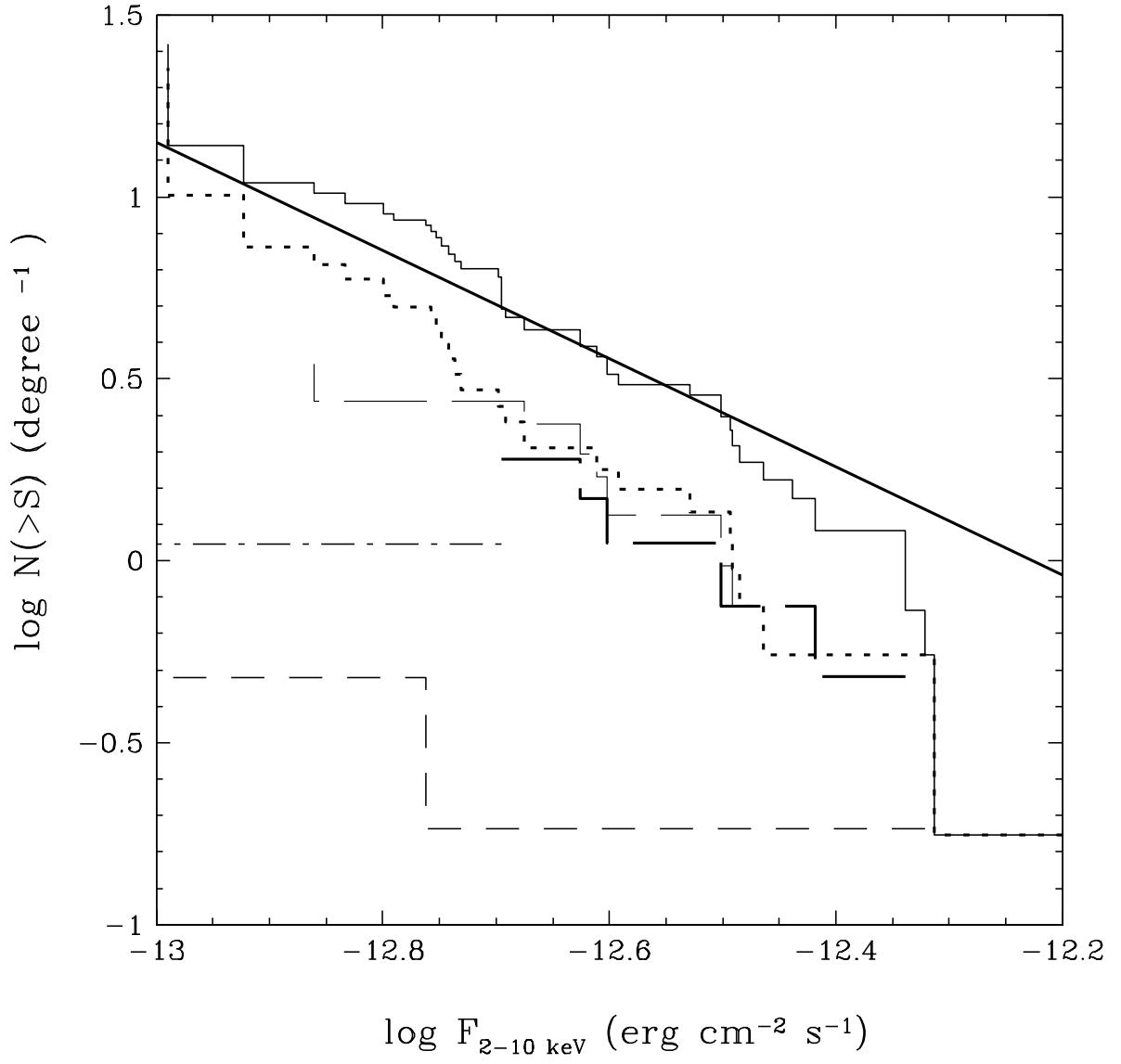


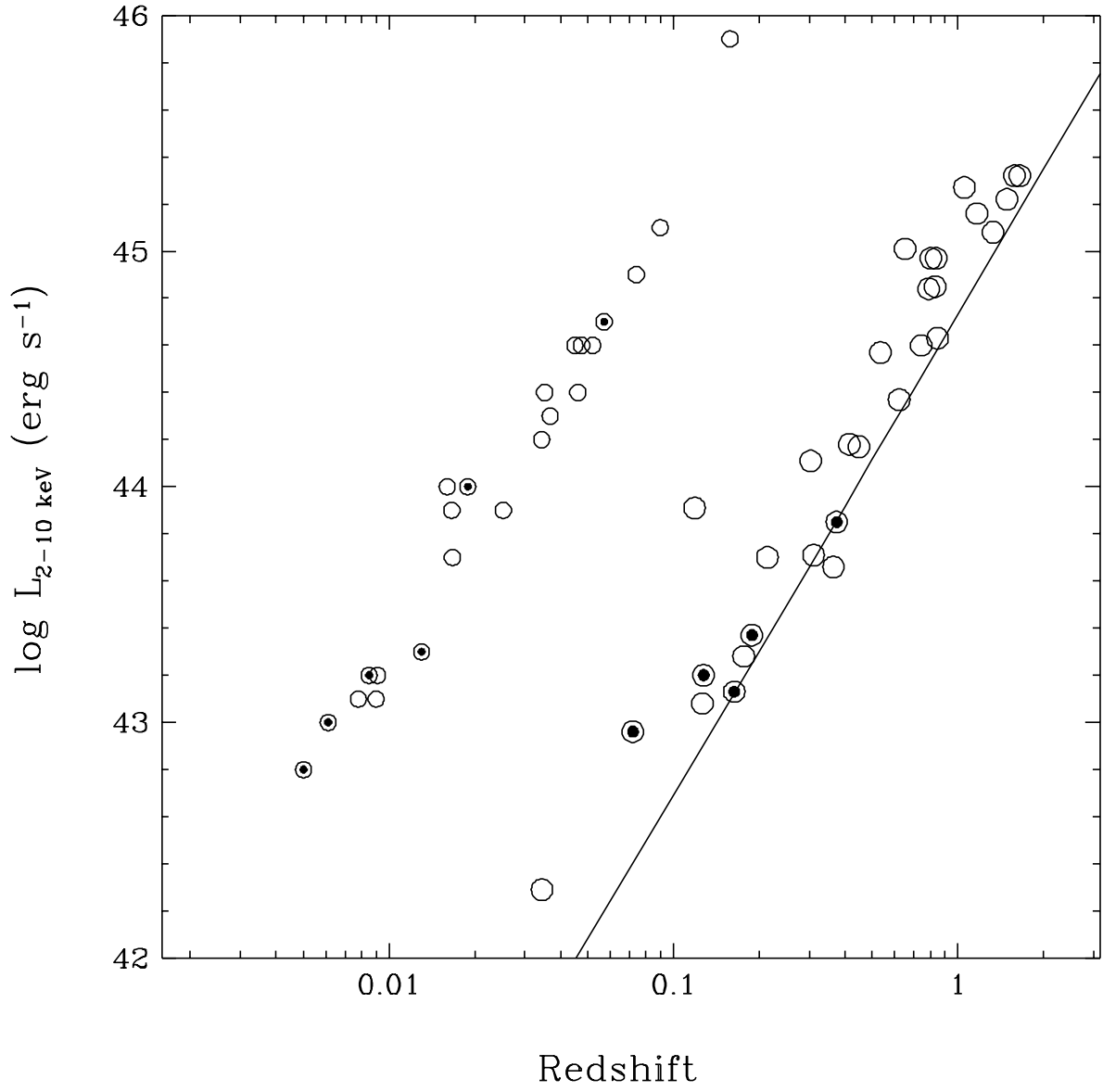


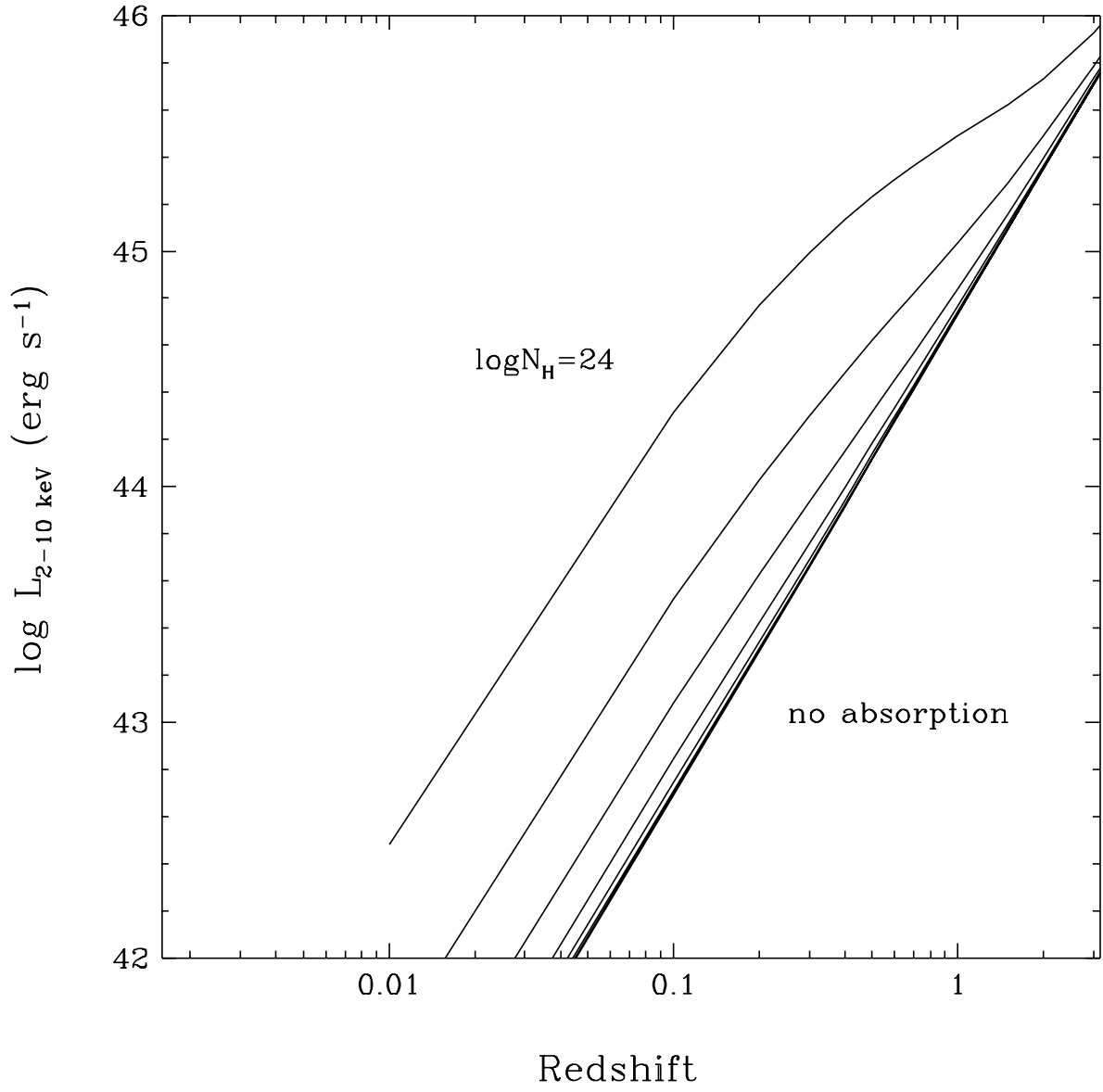


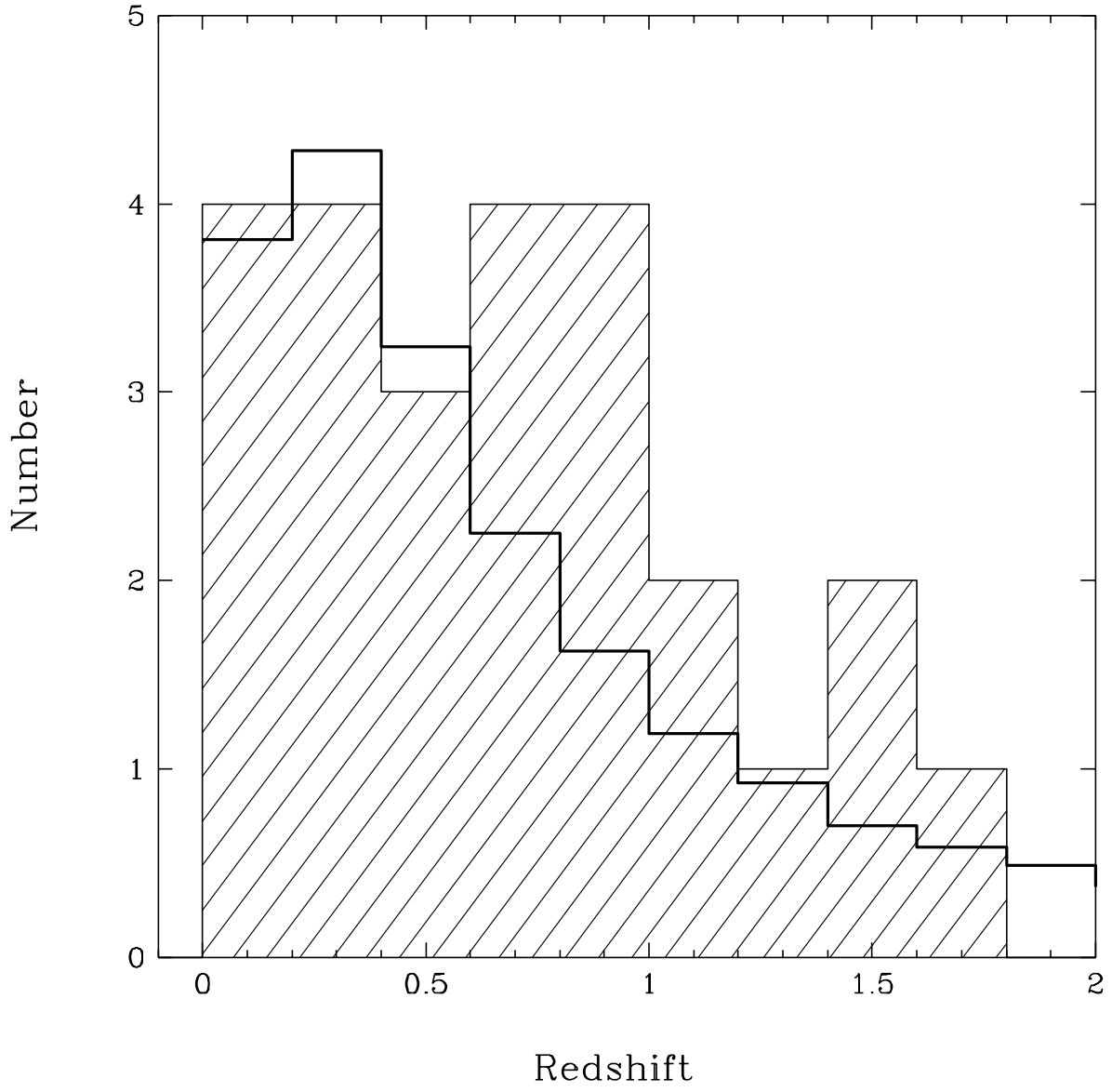


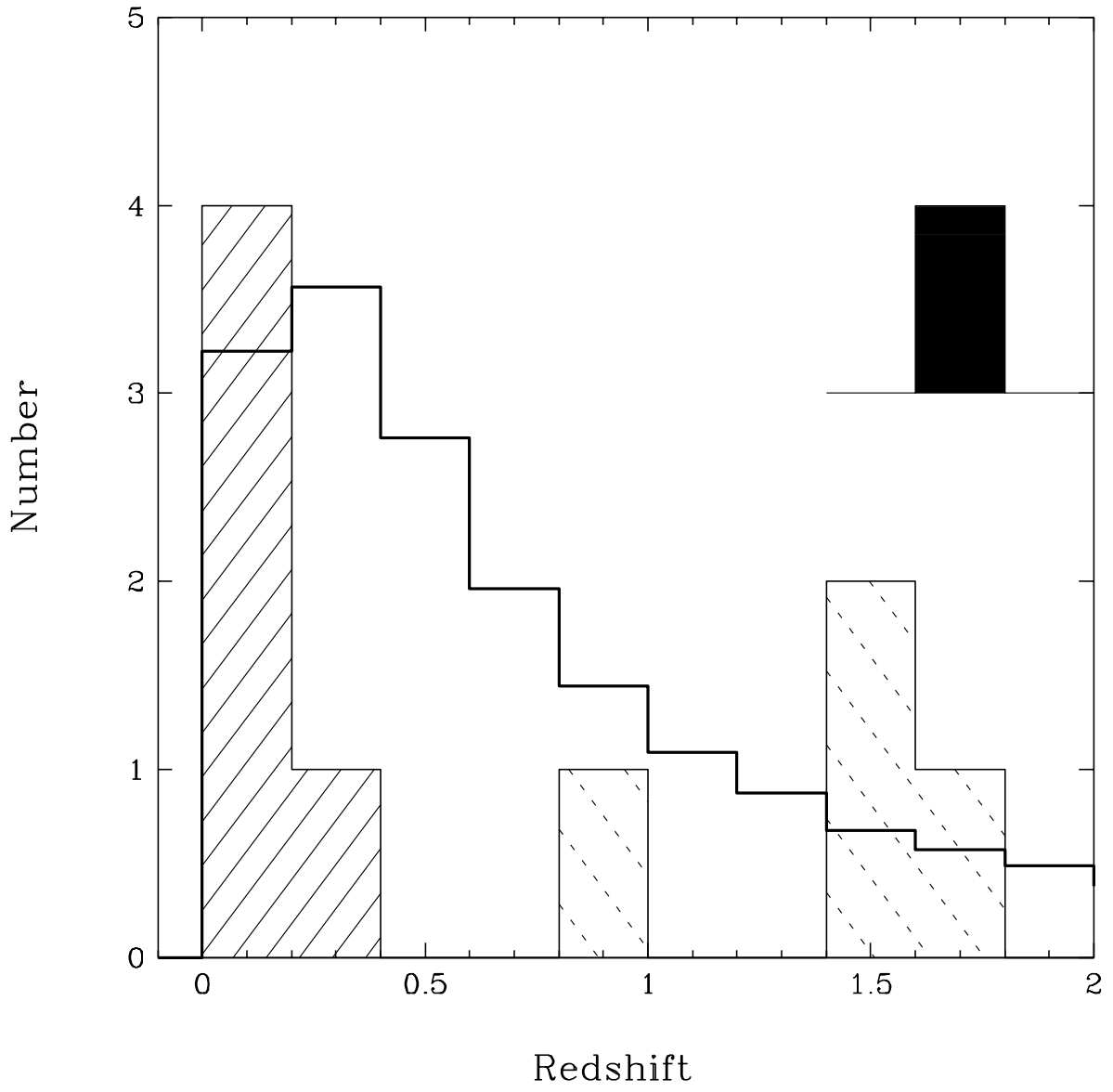


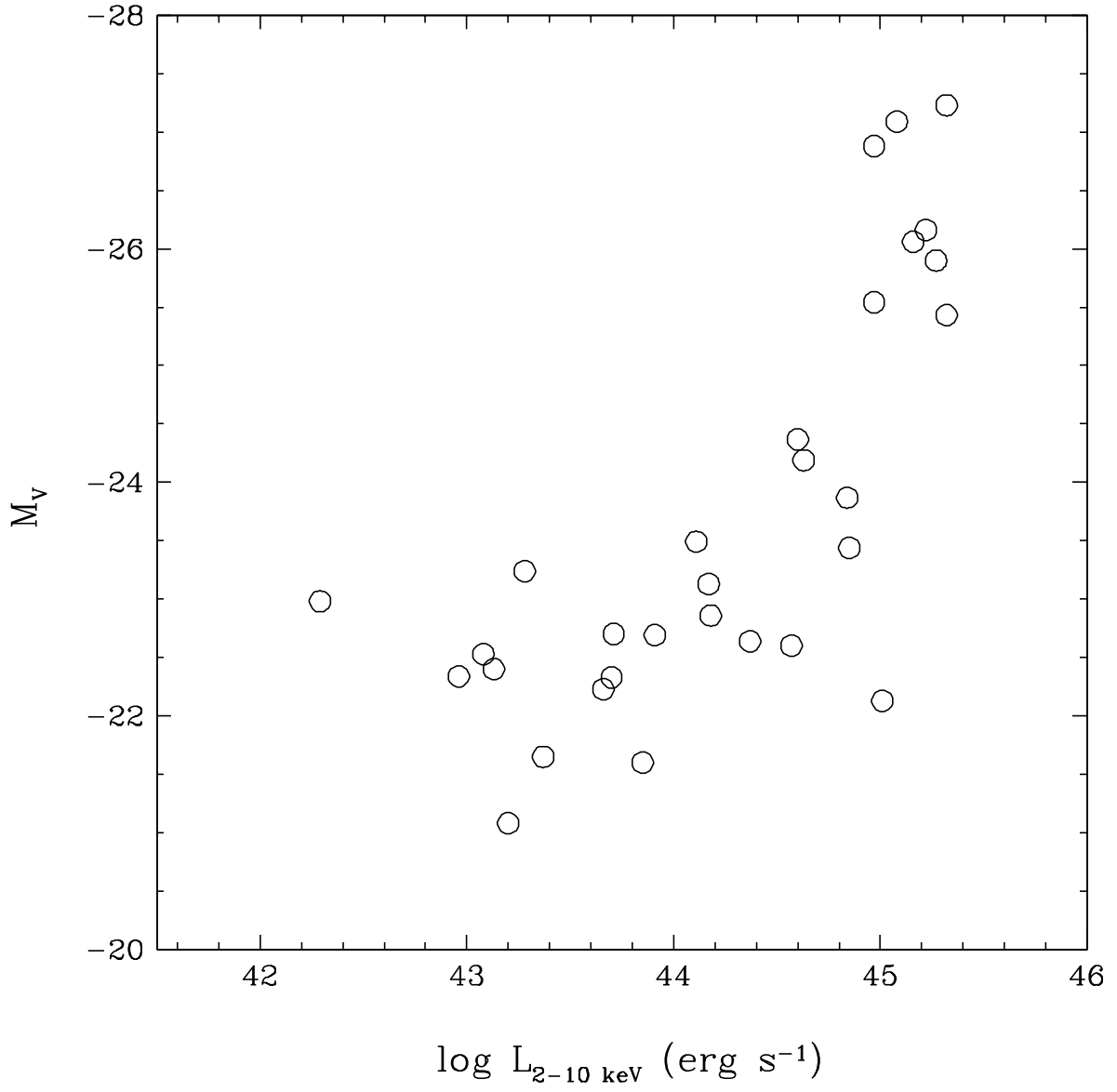


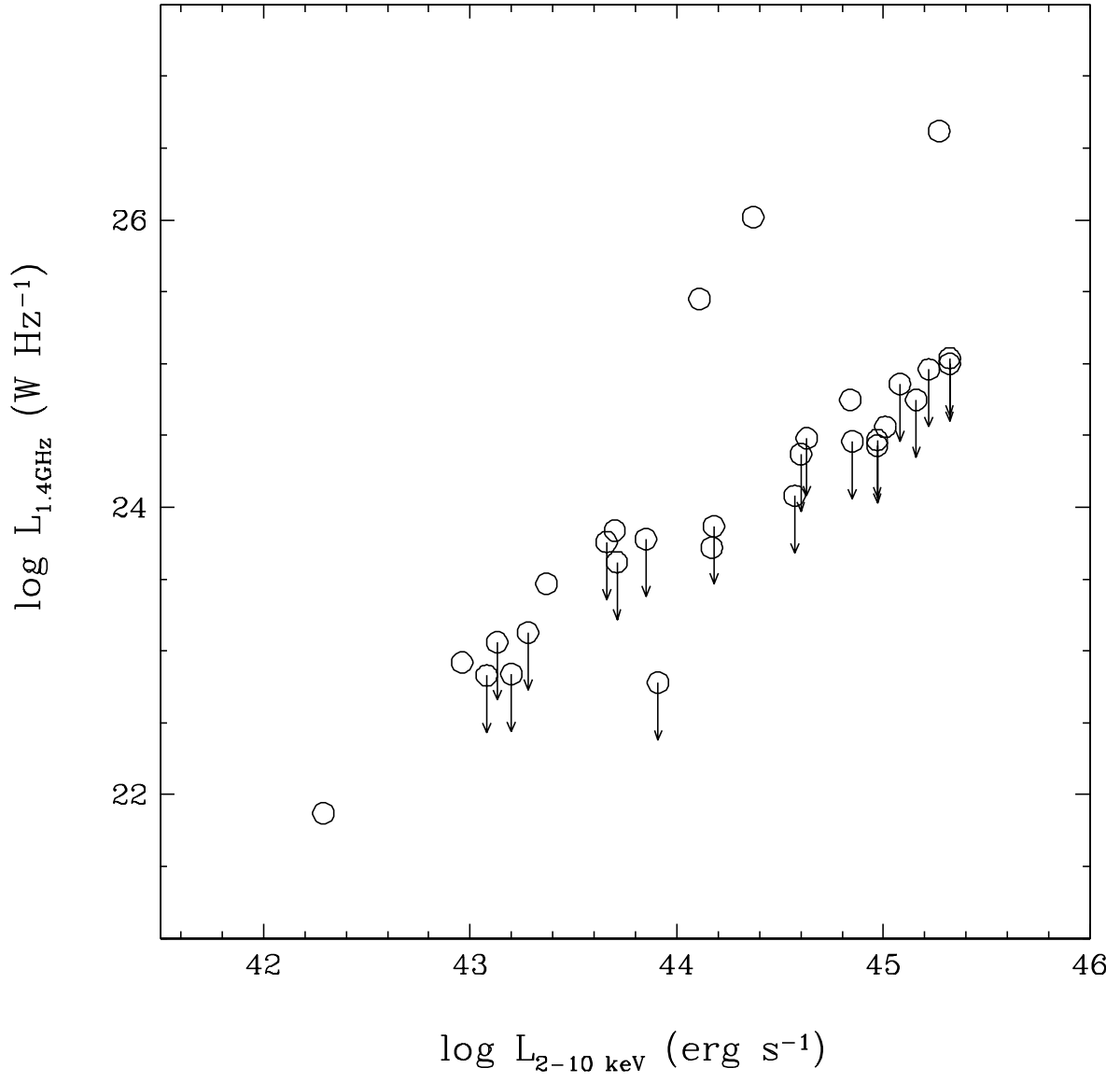












This figure "Figure1a.jpg" is available in "jpg" format from:

<http://arxiv.org/ps/astro-ph/0001289v1>

This figure "Figure1b.jpg" is available in "jpg" format from:

<http://arxiv.org/ps/astro-ph/0001289v1>

This figure "Figure1c.jpg" is available in "jpg" format from:

<http://arxiv.org/ps/astro-ph/0001289v1>

This figure "Figure1d.jpg" is available in "jpg" format from:

<http://arxiv.org/ps/astro-ph/0001289v1>

This figure "Figure1e.jpg" is available in "jpg" format from:

<http://arxiv.org/ps/astro-ph/0001289v1>

This figure "Figure1f.jpg" is available in "jpg" format from:

<http://arxiv.org/ps/astro-ph/0001289v1>

This figure "Figure1g.jpg" is available in "jpg" format from:

<http://arxiv.org/ps/astro-ph/0001289v1>

This figure "Figure1h.jpg" is available in "jpg" format from:

<http://arxiv.org/ps/astro-ph/0001289v1>

This figure "Figure1i.jpg" is available in "jpg" format from:

<http://arxiv.org/ps/astro-ph/0001289v1>

TABLE 2
CANDIDATES OF OPTICAL COUNTERPARTS AND RESULTS OF IDENTIFICATIONS

Name	No.	σ^a	Coordinate (J2000)			Offset (')	R^c (mag)	$B - R^c$ (mag)	Selection ^d	Classification	z		
			X-ray	No. ^b	Optical								
AX J131822+3347	235	10.0	13 18 22.92	33 47 41.6	A	13 18 23.75	33 47 36.6	0.19	16.35	0.91	P,B	AGN ^e	0.1186
AX J131850+3326	219	9.4	13 18 50.66	33 26 10.0	A	13 18 52.12	33 26 17.9	0.33	9.92	1.97	P	K-type star ^f	
AX J131345+3118	104	7.1	13 13 45.24	31 18 22.7	A	13 13 44.16	31 18 31.2 ^g	0.27	19.26 ^h	...	H ⁱ ,P,F	AGN	0.7887
AX J131249+3112	096	6.3	13 12 49.34	31 12 59.4	A	13 12 48.80	31 13 00.6	0.12	17.85	0.77	H,F,U,B	AGN ⁱ	1.0549
					B	13 12 51.37	31 13 08.4	0.46	18.17	0.93	B	...	
AX J131831+3341	228	5.7	13 18 31.27	33 41 45.6	A	13 18 31.59	33 41 45.3	0.07	20.60 ^k	1.12 ^k	P,F	AGN	0.6529
					B	13 18 33.27	33 41 07.7	0.76	18.74	1.00	B	...	
AX J131758+3257	195	5.5	13 17 58.87	32 57 48.6	A	13 18 00.20	32 57 52.1	0.28	17.99 ^k	1.77 ^k	P,F	AGN	0.2138
					B	13 17 56.89	32 58 00.8	0.46	18.12	0.82	B	Early-type star	
					Z	13 18 00.29	32 57 58.8	0.34	16.44	3.87	...	Late-type star	
AX J131816+3240	183	5.5	13 18 16.08	32 40 56.3	A	13 18 17.59	32 40 53.3	0.32	17.46 ^k	0.55 ^k	B	AGN	1.6487
AX J131551+3237	171	5.5	13 15 51.60	32 37 30.7 ^l	A	13 15 50.34	32 37 37.0	0.29	18.12 ^k	1.62 ^k	Br	AGN	0.1275
					Z	13 15 51.66	32 37 33.4	0.05	20.17 ^k	1.29 ^k	...	HII galaxy	0.2135
AX J131805+3349	233	5.5	13 18 05.78	33 49 28.9	A	13 18 05.37	33 49 36.9	0.16	13.38	0.44	F,U,B	AGN	0.0345
					B	13 18 08.43	33 49 27.6	0.55	16.58	1.26	P	...	
					C	13 18 02.73	33 49 51.9	0.74	14.55	0.78	U,B	...	
AX J131054+3004	037	5.2	13 10 54.17	30 04 08.0	A	13 10 55.11	30 04 11.5	0.21	17.68	2.01	F	AGN	0.2449
					B	13 10 53.43	30 04 30.0 ^g	0.40	19.17	0.73	B	AGN	1.5774
AX J131831+3320	212	5.2	13 18 31.73	33 20 30.1	A	13 18 31.63	33 20 36.6	0.11	19.70	0.72	P,B	AGN	0.5350
AX J131724+3203	152	4.9	13 17 24.31	32 03 24.1	A	13 17 24.06	32 03 45.5	0.36	18.20	0.46	B	HII galaxy	0.0586
					B	13 17 25.98	32 02 59.9	0.54	19.10	0.55	B	AGN	0.8489
AX J131521+3159	136	4.7	13 15 21.41	31 59 13.6	A	13 15 20.93	31 59 21.5 ^g	0.17	17.72 ^m	...	H,P,U	AGN	0.8382
AX J131021+3019	039	4.6	13 10 21.53	30 19 40.8	A	13 10 24.57	30 19 28.3	0.69	18.32	0.52	B	AGN ⁿ	1.4886
					Z	13 10 22.00	30 19 50.6	0.19	19.42 ^h	2.13 ^k	...	No emission line	
AX J131639+3149	137	4.6	13 16 39.22	31 49 38.6	A	13 16 37.91	31 49 52.1	0.36	19.98	-0.01	F ^o B	AGN	0.6218
					B	13 16 36.70	31 49 43.3	0.54	18.96	0.80	B	Early-type star	
AX J132032+3326	227	4.5	13 20 32.14	33 26 33.4	A	13 20 31.25	33 26 26.9	0.21	18.28	...	F,E	Cluster	...
AX J131501+3141	119	4.5	13 15 00.91	31 41 28.0 ^l	A	13 15 01.15	31 41 28.1 ^g	0.05	15.62 ^k	1.63 ^k	F	AGN	0.072
AX J131156+3054	075	4.4	13 11 56.50	30 54 43.2	A	13 11 56.41	30 54 47.3	0.07	19.25	1.12	P	AGN	0.3656
AX J131725+3300	192	4.4	13 17 25.58	33 00 03.2	A	13 17 26.99	33 00 22.6	0.44	16.64	2.25	P	AGN	0.1261
AX J131407+3158	127	4.3	13 14 07.25	31 58 30.0	A	13 14 06.40	31 58 44.1	0.30	16.66	1.45	H,P	AGN	0.1766
AX J130748+2925	002	4.3	13 07 48.82	29 25 58.1	A	13 07 49.30	29 25 47.8 ^g	0.20	16.34 ^h	...	F,P,E	Cluster ^p	0.241
AX J131327+3155	121	4.1	13 13 27.22	31 55 25.3	A	13 13 27.45	31 55 20.8 ^g	0.09	17.58 ^h	...	H,F,U	AGN ^p	0.3033
AX J131832+3259	199	4.1	13 18 32.18	32 59 14.3	A	13 18 29.98	32 58 45.9	0.66	16.79	1.24	Br	G-type star	
AX J131529+3117	110	4.0	13 15 29.02	31 17 32.6	A	13 15 28.58	31 17 43.4	0.20	18.79	0.14	P,F ^o ,U,B	AGN	0.4485
AX J131927+3343	238	4.0	13 19 27.14	33 43 12.4	A	13 19 27.16	33 43 12.9	0.01	18.90 ^k	0.60 ^k	P,B	AGN	0.4156
AX J130926+2952	016	4.0	13 09 29.04	29 52 01.2 ^l	A	13 09 28.29	29 52 11.1	0.23	19.93 ^k	1.94 ^k	P	AGN	0.3751
					B	13 09 26.31	29 51 36.1	0.73	14.16	1.00	B	...	
AX J131707+3237	175	3.9	13 17 07.80	32 37 22.4	A	13 17 09.54	32 37 13.5	0.40	18.64	0.88	B	AGN	0.7446
					B	13 17 09.75	32 38 02.4	0.78	16.31	0.99	B	...	
AX J131210+3048	072	3.7	13 12 12.72	30 48 21.2 ^l	A	13 12 12.00	30 48 21.4 ^g	0.15	18.40 ^k	2.05 ^k	F	AGN	0.1888
AX J130840+2955	014	3.7	13 08 40.73	29 55 27.1	A	13 08 41.31	29 55 47.4	0.36	17.34	1.81	Br	AGN	0.1635
AX J131128+3105	080	3.6	13 11 28.70	31 05 43.1	A	13 11 28.41	31 05 51.7	0.16	17.15	0.54	H,P,U,B	AGN	1.3314
					B	13 11 27.34	31 05 43.4	0.29	19.31	0.02	U,B	...	
AX J131321+3119	103	3.6	13 13 21.07	31 19 30.0	A	13 13 20.46	31 19 21.6	0.19	19.81	-0.19	H,U,B	AGN	0.8338
AX J131928+3251	197	3.6	13 19 28.37	32 51 03.2	A	13 19 29.89	32 50 45.6	0.43	18.43	0.95	B	AGN	0.3107
AX J131015+3004	033	3.5	13 10 15.26	30 04 19.2	A	13 10 16.01	30 04 16.8	0.17	17.90	1.01	P,U	AGN	1.1651
AX J130826+3005	023	3.5	13 08 26.42	30 05 40.6	A	13 08 29.66	30 05 39.1	0.70	16.29	0.77	P,U,B	AGN ^r	0.8033

^aDetection significances in the SIS 2–7 keV band.

^bIdentification numbers of optical objects in figure 1. A, B, and C are selected targets in order of a distance from an X-ray center. Z is an additional object which was spectroscopically observed.

^cCoordinates and magnitudes are taken from APM catalog (McMahon et al. 1992), except for objects with notes.

^dSelection methods of candidates of optical counterparts. H:ROSAT HRI, P:ROSAT PSPC (Voges et al. 1998), F:FIRST (Becker, White, & Helfand 1995), E:Galaxy excess, U:UV excess (Usher 1981; Moreau & Reboul 1995; Takase & Miyauchi-Isobe 1986), B:Blue color, Br:Brightest object in the error circle. For detail, see section 2.2.

^eAlready cataloged in Bade et al. (1998)

^fAlready cataloged as HD115781.

^gCoordinate determined by CCD image taken during the spectroscopic observations.

^hDetermined by relative photometry with mosaic CCD image taken at KISO observatory.

ⁱIn the ROSAT HRI image, there is an X-ray peak whose significance level is slightly lower than the detection limit.

^jAlready cataloged in Falco, Kochanek, & Munoz (1998).

^kDetermined by CCD photometry done at University of Hawaii 88" telescope in March 1996 and March 1999.

^lX-ray positions were determined by deep pointing observations by ASCA (Sakano et al. 1998; Sakano et al. 1999; Ueda et al. 1999b).

^mAPM magnitude data is blended. Deblending was done using CCD image taken during the spectroscopic observations.

ⁿAlready cataloged in Schade (1991).

^oThe nearest object to a FIRST radio source. The radio source is 14" offsetted from the optical object. See section 3.1.

^pIdentified in the *Einstein* Medium Sensitivity Survey (Stoche et al. 1991).

^qIn the FIRST radio map, there is a radio peak whose significance level is slightly lower than the detection limit.

^rAlready cataloged in Wills & Wills (1976).

TABLE 3
OPTICAL SPECTRAL PROPERTIES OF THE LSS AGNs

Name	No.	z	Detected Broad Lines	H α FWHM ^a (km s ⁻¹)	H β FWHM ^a (km s ⁻¹)	MgII FWHM ^a (km s ⁻¹)	log(H α /[NII]) ^b	log(H β /[OIII]) ^c	MgII EW (Å)
AX J131822+3347	235	0.1186	H δ ,H γ ,H β ,H α	569,3397 ^d	867,5233 ^d	...	1.31 ^{+0.08} _{-0.07}	0.52 ^{+0.07} _{-0.08}	...
AX J131345+3118	104	0.7887	MgII 2800Å	9695	83
AX J131249+3112	096	1.0549	MgII 2800Å	6854	29
AX J131831+3341	228	0.6529	MgII 2800Å	...	849	8684	...	-0.54 ^{+0.53} _{-0.73}	99
AX J131758+3257	195	0.2138	Only Narrow Line	666	768	...	0.28 ^{+0.55} _{-0.29}	<-0.63	...
AX J131816+3240	183	1.6487	CIII] 1909Å,MgII 2800Å	6949	33
AX J131551+3237	171	0.1275	Only Narrow Line	<486	<657	...	0.35 ^{+0.12} _{-0.14}	-0.45 ^{+0.10} _{-0.15}	...
AX J131805+3349	233	0.0345	H α	<530,5817 ^d	1.03 ^{+0.11} _{-0.10}	<-0.63	...
AX J131054+3004	037	1.5774	CIII] 1909Å,MgII 2800Å	6136	50
AX J131831+3320	212	0.5350	MgII 2800Å,H γ ,H β	...	647,9988 ^d	0.55 ^{+0.09} _{-0.09}	...
AX J131724+3203	152	0.8489	MgII 2800Å	7804	69
AX J131521+3159	136	0.8382	MgII 2800Å	6661	29
AX J131021+3019	039	1.4886	CIII] 1909Å,MgII 2800Å	1999	17
AX J131639+3149	137	0.6218	MgII 2800Å	8486	59
AX J131501+3141	119	0.072	Only Narrow Line	325	325	...	0.06 ^{+0.10} _{-0.10}	-0.65 ^{+0.10} _{-0.10}	...
AX J131156+3054	075	0.3656	H β	...	<542,4711 ^d	0.33 ^{+0.31} _{-0.18}	...
AX J131725+3300	192	0.1261	H α	<487,4966 ^d	<658	...	1.18 ^{+0.26} _{-0.23}	-0.34 ^{+0.25} _{-0.16}	...
AX J131407+3158	127	0.1766	H β ,H α	<466,3196 ^d	3984	...	0.82 ^{+0.12} _{-0.11}	-0.46 ^{+0.11} _{-0.14}	...
AX J131327+3155	121	0.3033	H β	...	4088	0.29 ^{+0.16} _{-0.17}	...
AX J131529+3117	110	0.4485	H δ ,H γ ,H β	...	840,4094 ^d	0.20 ^{+0.05} _{-0.06}	...
AX J131927+3343	238	0.4156	H δ ,H γ ,H β	...	<523,3711 ^d	0.15 ^{+0.06} _{-0.07}	...
AX J130926+2952	016	0.3751	H β	...	696,1791 ^d	-0.59 ^{+0.18} _{-0.34}	...
AX J131707+3237	175	0.7446	MgII 2800Å	1485,7886 ^d	...	0.45 ^{+0.55} _{-0.52}	25 ^d
AX J131210+3048	072	0.1888	Only Narrow Line	<461	<630	...	0.08 ^{+0.40} _{-0.09}	<-0.53	...
AX J130840+2955	014	0.1635	Only Narrow Line	<-0.63	...
AX J131128+3105	080	1.3314	CIII] 1909Å,MgII 2800Å	7807	29
AX J131321+3119	103	0.8338	MgII 2800Å	8073	41
AX J131928+3251	197	0.3107	H γ ,H β	...	2946	-0.29 ^{+0.09} _{-0.10}	...
AX J131015+3004	033	1.1651	MgII 2800Å	5859	25
AX J130826+3005	023	0.8033	MgII 2800Å	4854	17

^aFWHMs are corrected for the instrumental broadening with the spectral resolution of 12Å.

^bLogarithmic equivalent width ratio of broad-plus narrow-H α lines-to-narrow [NII]6583Å line.

^cLogarithmic equivalent width ratio of broad-plus narrow-H β lines-to-narrow [OIII]5007Å line.

^dFitted with 2 components.

TABLE 4
PHYSICAL PARAMETERS OF THE SAMPLE

Name	No.	P.I. ^a	F_{XH}^{b}	L_{XH}^{c}	F_{XS}^{d}	L_{XS}^{e}	N_{H}^{f}	R	M_{V}^{g}	$S_{\text{peak}}^{\text{h}}$	L_{R}^{i}	Classification	z	Notes ^j
AX J131822+3347	235	2.08 ± 0.07	12.71	43.91	9.20	43.77	<0.0056	16.35	-22.69	...	<22.78	AGN	0.1186	S+D
AX J131850+3326	219	2.65 ± 0.09	3.10	...	5.16	9.92	K-type star	...	S
AX J131345+3118	104	1.69 ± 0.14	2.39	44.84	1.22	44.55	$0.005^{+0.419}_{-0.005}$	19.26	-23.87	2.13	24.75	AGN	0.7887	S
AX J131249+3112	096	1.62 ± 0.13	3.70	45.27	1.47	44.87	$0.345^{+0.632}_{-0.345}$	17.85	-25.90	90.08 ^k	26.62	AGN	1.0549	S
AX J131831+3341	228	1.45 ± 0.14	5.81	45.01	2.01	44.55	$0.583^{+0.443}_{-0.416}$	20.60	-22.13	2.03	24.56	AGN	0.6529	S+D
AX J131758+3257	195	1.64 ± 0.15	2.47	43.70	0.93	43.27	$0.045^{+0.192}_{-0.045}$	17.99	-22.33	3.51	23.84	AGN	0.2138	G
AX J131816+3240	183	1.33 ± 0.16	2.24	45.32	0.55	44.72	$3.217^{+1.958}_{-1.758}$	17.46	-27.23	...	<25.04	AGN	1.6487	S
AX J131551+3237	171	0.32 ± 0.34	2.61	43.20	0.15	41.95	$1.9^{+1.31}_{-1.0}$	18.12	-21.08	...	<22.84	AGN	0.1275	G
AX J131805+3349	233	1.68 ± 0.21	3.80	42.29	1.98	42.01	$0.134^{+0.185}_{-0.134}$	13.38	-22.98	1.46	21.87	AGN	0.0345	G
AX J131054+3004	037	1.58 ± 0.19	1.91	45.32	0.98	45.03	$1.685^{+2.008}_{-1.685}$	19.17	-25.43	...	<25.00	AGN	1.5774	S
AX J131831+3320	212	1.83 ± 0.11	2.63	44.57	0.92	44.11	<0.218	19.70	-22.60	...	<24.08	AGN	0.5350	S
AX J131724+3203	152	1.23 ± 0.22	1.67	44.63	0.50	44.11	$1.588^{+1.074}_{-0.945}$	19.10	-24.19	...	<24.48	AGN	0.8489	S
AX J131521+3159	136	1.86 ± 0.16	2.55	44.97	1.30	44.68	<0.191	17.72	-25.54	...	<24.47	AGN	0.8382	S
AX J131021+3019	039	1.24 ± 0.21	2.31	45.22	0.54	44.59	$5.120^{+2.642}_{-2.257}$	18.32	-26.16	...	<24.96	AGN	1.4886	S
AX J131639+3149	137	1.72 ± 0.21	1.30	44.37	0.59	44.03	$0.070^{+0.508}_{-0.070}$	19.98	-22.64	64.55	26.02	AGN	0.6218	S
AX J132032+3326	227	1.96 ± 0.16	2.56	...	1.60	18.28	...	18.44 ^k	24.50	Cluster	...	
AX J131501+3141	119	-0.68 ± 0.45	4.78	42.96	0.06	41.09	$6.4^{+3.11}_{-2.3}$	15.62	-22.34	3.74	22.92	AGN	0.072	G
AX J131156+3054	075	1.55 ± 0.26	0.79	43.66	0.49	43.45	$0.197^{+0.439}_{-0.197}$	19.25	-22.23	...	<23.76	AGN	0.3656	S
AX J131725+3300	192	1.52 ± 0.21	1.74	43.08	0.44	42.48	$0.247^{+0.243}_{-0.221}$	16.64	-22.53	...	<22.83	AGN	0.1261	G
AX J131407+3158	127	1.76 ± 0.23	1.37	43.28	0.87	43.08	<0.194	16.66	-23.24	...	<23.13	AGN	0.1766	G
AX J130748+2925	002	1.96 ± 0.16	4.14	44.06	2.93	43.91	...	16.34	...	2.80	23.84	Cluster	0.241	
AX J131327+3155	121	1.76 ± 0.17	3.05	44.11	1.24	43.72	<0.165	17.58	-23.49	72.24 ^k	25.45	AGN	0.3033	S
AX J131832+3259	199	0.58 ± 0.35	1.41	...	0.19	No ID	...	
AX J131529+3117	110	2.11 ± 0.23	1.37	44.17	1.34	44.16	<0.101	18.79	-23.13	0.63	23.72	AGN	0.4485	S
AX J131927+3343	238	1.48 ± 0.21	2.09	44.18	0.61	43.65	$0.365^{+0.443}_{-0.365}$	18.90	-22.86	...	<23.87	AGN	0.4156	S
AX J130926+2952	016	0.81 ± 0.30	1.47	43.85	0.16	42.88	$2.3^{+1.81}_{-1.2}$	19.93	-21.60	...	<23.78	AGN	0.3751	G
AX J131707+3237	175	1.95 ± 0.24	1.32	44.60	0.93	44.44	<0.240	18.64	-24.37	...	<24.37	AGN	0.7446	S
AX J131210+3048	072	0.76 ± 0.31	1.76	43.37	0.28	42.57	$1.1^{+0.91}_{-0.6}$	18.40	-21.65	1.92	23.47	AGN	0.1888	G
AX J130840+2955	014	0.34 ± 0.44	1.39	43.13	0.15	42.16	$2.857^{+1.191}_{-1.114}$	17.34	-22.40	...	<23.06	AGN	0.1635	G
AX J131128+3105	080	1.65 ± 0.24	1.41	45.08	0.36	44.49	<1.430	17.15	-27.09	...	<24.86	AGN	1.3314	S
AX J131321+3119	103	1.54 ± 0.18	2.36	44.85	0.71	44.33	$0.252^{+0.695}_{-0.252}$	19.81	-23.44	...	<24.46	AGN	0.8338	S
AX J131928+3251	197	1.65 ± 0.26	1.19	43.71	0.50	43.33	$0.055^{+0.386}_{-0.055}$	18.43	-22.70	...	<23.62	AGN	0.3107	G
AX J131015+3004	033	1.70 ± 0.19	2.17	45.16	0.81	44.73	<0.622	17.90	-26.06	...	<24.75	AGN	1.1651	S
AX J130826+3005	023	1.83 ± 0.17	2.84	44.97	1.56	44.71	<0.334	16.29	-26.88	...	<24.43	AGN	0.8033	S

^aX-ray power-law photon index determined in the 0.7–10 keV band with GIS and SIS.

^b2–10 keV flux in 10^{-13} erg cm⁻² s⁻¹ derived from the GIS data. Conversions from count rates were done based on the best fit power-law indices.

^cLogarithmic 2–10 keV luminosity in erg s⁻¹. K-correction was made with the measured photon index.

^d0.5–2 keV flux in 10^{-13} erg cm⁻² s⁻¹ derived from the GIS data. Conversions from count rates were done based on the best fit power-law indices.

^eLogarithmic 0.5–2 keV luminosity in erg s⁻¹. K-correction was made with the measured photon index.

^fThe best-fit intrinsic column densities from absorption fitting in unit of 10^{22} cm⁻². The intrinsic photon index of 1.7 and the absorption at the object redshift are assumed. The errors indicate 1σ error regions.

^gOptical V-band absolute magnitude derived in assumption of optical power-law index of -0.5 which corresponds to $V - R$ color of 0.22mag.

^hRadio peak flux at 1.4GHz in mJy from FIRST radio catalog.

ⁱLogarithmic radio luminosity at 1.4GHz in W Hz⁻¹. K-correction was made with power-law index of -0.5 . Upper limit was estimated using the flux limit of 1mJy.

^jNotes on optical images of the objects. S:Stellar, S+D:Stellar component with faint nebulosity, and G:Galaxy.

^kSummed flux of multi components.

^lDetermined from deep follow-up observations with *ASCA* (Sakano et al. 1998; Sakano et al. 1999; Ueda et al. 1999b).

TABLE 6
ROSAT HRI SOURCES IN FIELD 1 AND 2

Name	Coordinate (J2000.0) X-ray		ML ^a	Count Rate ^a (cts ksec ⁻¹)	Coordinate (J2000.0) Optical		R^b	$B - R^b$	Notes
LSS1-01	13 14 58.25	32 07 49.8	76.2	2.64 ± 0.41	13 14 58.11	32 07 48.4	19.48	0.34	
LSS1-02	13 13 29.80	32 06 05.9	10.5	1.59 ± 0.46	13 13 29.39	32 06 07.4	19.83	1.80	
LSS1-03	13 14 41.89	32 05 19.0	15.0	0.61 ± 0.20	13 14 41.80	32 05 17.4	19.67	0.79	
LSS1-04	13 14 09.48	32 03 04.3	10.0	0.61 ± 0.22	13 14 09.82	32 03 00.5	18.55	2.50	
LSS1-05	13 15 11.28	32 02 32.2	219.8	5.20 ± 0.56	13 15 11.12	32 02 29.3	18.99	0.54	
LSS1-06	13 15 21.12	31 59 22.5	401.8	10.13 ± 0.79	13 15 20.93	31 59 21.5 ^c	17.72	...	AX J131521+3159(136)
LSS1-07	13 14 06.31	31 58 45.3	169.8	4.37 ± 0.52	13 14 06.40	31 58 44.1	16.66	1.45	AX J131407+3158(127)
LSS1-08	13 15 10.70	31 57 17.7	23.4	1.29 ± 0.31	13 15 10.69	31 57 28.1	16.76	0.94	
LSS1-09	13 15 03.38	31 56 22.8	29.2	1.25 ± 0.29	13 15 03.32	31 56 21.4	18.93	0.96	
LSS1-10	13 13 27.06	31 55 18.8	37.3	4.02 ± 0.66	13 13 27.45	31 55 20.8 ^c	17.58	...	AX J131327+3155(121)
LSS1-11	13 14 39.07	31 50 33.5	11.4	1.00 ± 0.31	13 14 39.25	31 50 33.8 ^c	
LSS2-01	13 12 42.47	31 20 32.1	24.3	1.20 ± 0.30	13 12 42.77	31 20 30.5	11.42	...	
LSS2-02	13 13 20.43	31 19 24.5	10.7	1.40 ± 0.41	13 13 20.46	31 19 21.6	19.81	-0.19	AX J131321+3119(103)
LSS2-03	13 12 34.35	31 18 54.2	16.0	0.73 ± 0.23	13 12 34.36	31 18 52.1	20.89	...	
LSS2-04	13 12 21.29	31 17 52.2	121.1	3.20 ± 0.46	13 12 21.26	31 17 50.7	18.13	0.12	
LSS2-05	13 12 43.75	31 17 31.6	16.7	0.78 ± 0.24	13 12 43.59	31 17 28.0 ^c	
LSS2-06	13 11 30.01	31 16 04.3	13.9	1.54 ± 0.42	13 11 30.18	31 16 07.0	18.69	0.00	
LSS2-07	13 12 48.92	31 13 00.6	456.2	9.29 ± 0.77	13 12 48.80	31 13 00.6	17.85	0.77	AX J131249+3112(096)
LSS2-08	13 12 54.80	31 12 26.5	11.9	0.66 ± 0.23	13 12 54.92	31 12 22.7	2 objects blended
LSS2-09	13 12 36.28	31 08 26.6	31.1	1.17 ± 0.29	13 12 36.41	31 08 26.2	
LSS2-10	13 12 21.15	31 08 24.1	28.6	1.19 ± 0.30	13 12 21.08	31 08 24.8 ^c	
LSS2-11	13 11 58.49	31 07 53.4	10.2	0.87 ± 0.29	13 11 58.52	31 07 57.6	19.78	1.30	
LSS2-12	13 12 47.79	31 07 43.1	14.8	0.79 ± 0.25	13 12 47.70	31 07 44.1	
LSS2-13	13 11 28.49	31 05 47.3	16.6	3.17 ± 0.70	13 11 28.41	31 05 51.7	17.15	0.54	AX J131128+3105(080)
LSS2-14	13 13 21.77	31 00 17.0	25.5	4.36 ± 0.80	13 13 21.51	31 00 19.6	19.71	0.19	

^aMaximum likelihoods and count rates in the PHS channel range from 2 to 8, only.

^bCoordinates and magnitudes are taken from APM catalog (McMahon et al. 1992), except for objects with notes.

^cCoordinates determined by mosaic CCD image taken at KISO observatory.

TABLE 7
THE IDENTIFICATIONS OF THE *ASCA* LSS SOURCES WITH THE *ROSAT* PSPC SOURCES AND THE VLA
FIRST SOURCES

Name	No.	<i>ROSAT</i> PSPC	FIRST
AX J131822+3347	235	1RXS J131823.5+334745,1RXP J131824.5+334733	
AX J131850+3326	219	1RXS J131851.8+332653,1RXP J131852.1+332616	
AX J131345+3118	104	1RXP J131344.8+311841	FRS J131344.1+311829
AX J131249+3112	096		FRS J131248.7+311300,FRS J131249.4+311249
AX J131831+3341	228	1RXP J131832.1+334146	FRS J131831.6+334146
AX J131758+3257	195	1RXS J131759.6+325741	FRS J131800.2+325752
AX J131816+3240	183		
AX J131551+3237	171		
AX J131805+3349	233	1RXS J131807.5+334929	FRS J131805.2+334938
AX J131054+3004	037		FRS J131055.0+300410
AX J131831+3320	212	1RXS J131832.4+332019,1RXP J131831.5+332038	
AX J131724+3203	152		
AX J131521+3159	136	1RXS J131521.7+315930	
AX J131021+3019	039		
AX J131639+3149	137		FRS J131638.9+314956
AX J132032+3326	227		FRS J132033.4+332633,FRS J132031.1+332614 FRS J132033.8+332639,FRS J132030.9+332608
AX J131501+3141	119		FRS J131501.1+314129
AX J131156+3054	075	1RXP J131157.4+305448	
AX J131725+3300	192	1RXS J131725.7+330024,1RXP J131725.4+330018	
AX J131407+3158	127	1RXS J131405.5+315901	
AX J130748+2925	002	1RXS J130749.3+292536,1RXP J130748.7+292542	FRS J130749.2+292548
AX J131327+3155	121	1RXS J131325.4+315515	FRS J131327.3+315523,FRS J131328.2+315516
AX J131832+3259	199		
AX J131529+3117	110	1RXS J131528.9+311737,1RXP J131529.9+311733	
AX J131927+3343	238	1RXP J131925.9+334303	
AX J130926+2952	016	1RXS J130927.3+295204,1RXP J130927.7+295205	
AX J131707+3237	175		
AX J131210+3048	072		FRS J131211.9+304821
AX J130840+2955	014		
AX J131128+3105	080	1RXS J131128.9+310542,1RXP J131127.8+310539	
AX J131321+3119	103		
AX J131928+3251	197		
AX J131015+3004	033	1RXS J131016.3+300408	
AX J130826+3005	023	1RXS J130829.6+300536,1RXP J130829.8+300539	

^a1RXS and 1RXP mean sources from *ROSAT* PSPC All-Sky Survey Source Catalog (Voges et al. 1999) and *ROSAT* PSPC Pointing Catalog (Voges, private communication), respectively.